Enhanced efficiency and durability of nickel sulfide catalyst integrated with reduced graphene oxide

Exploring hierarchically porous structures for methanol oxidation reaction

Salmi, Mehdi; Khossossi, Nabil; Boudad, Yousra; Jama, Charafeddine; Bentiss, Fouad; Zaroual, Zaina; El Ghachtouli, Sanae

DOI
10.1016/j.ijhydene.2024.12.285

Publication date
2025

Document Version
Final published version

Published in
International Journal of Hydrogen Energy

International Journal of Hydrogen Energy 100 (2025) 580–595

Contents lists available at ScienceDirect

International Journal of Hydrogen Energy

journal homepage: www.elsevier.com/locate/he

Enhanced efficiency and durability of nickel sulfide catalyst integrated with reduced graphene oxide: Exploring hierarchically porous structures for methanol oxidation reaction

Mehdi Salmi [a,**], Nabil Khossossi [b], Yousra Boudad [a], Charafeddine Jama [c], Fouad Bentiss [c,d], Zaina Zaroual [a], Sanae El Ghachtouli [a,*]

[a] Laboratory of Interface Materials Environment, Faculty of Science Ain Chock – Hassan II University of Casablanca, Casablanca, Morocco
[b] Department of Materials Science and Engineering, Faculty of Mechanical, Maritime and Materials Engineering, Delft University of Technology, Mekelweg 2, Delft, 2628 CD, the Netherlands
[c] University. Lille, CNRS, INRAE, Central Lille, UMR 8207, UMET – Unité Matériaux et Transformation, F-59000, Lille, France
[d] Laboratoy of Catalysis and Corrosion of Materials, Faculty of Sciences, Chouaib Doukkali University, PO Box 20, M-24000, El Jadida, Morocco

ARTICLE INFO

Keywords:
Nickel sulfide
Methanol oxidation reaction
Dynamic hydrogen bubble template
Electrodeposition
Electrocatalysis
Density functional theory

ABSTRACT

The growing demand for sustainable energy solutions highlights the need for advancements in electrocatalysts for direct methanol fuel cells (DMFCs). This study introduces a novel approach to enhance the efficiency and durability of nickel sulfide (NiS) catalysts. We developed a hierarchically porous structure integrated with reduced graphene oxide (rGO) on a nickel foam substrate. Using a dynamic hydrogen bubble template (DHBT) technique, we created a porous nickel scaffold. We then electrodeposited graphene oxide and NiS onto this scaffold, resulting in a hybrid structure termed NiS-rGO-Ni/NF. Characterization through SEM, XRD, and XPS confirmed that the catalyst has a highly porous structure with uniformly distributed Ni_3S_2 and Ni_3S_4 phases. The NiS-rGO-Ni/NF catalyst showed significant improvements over conventional NiS/NF. It achieved a peak current density of 84.10 mA/cm^2 in the presence of 0.1 M methanol, compared to 30.32 mA/cm^2 with NiS/NF. This enhancement is due to the porous nickel layer created using DHBT and the integration of rGO. Additionally, the NiS-rGO-Ni/NF catalyst demonstrated superior reaction kinetics, evidenced by a decrease in the Tafel slope from 204 mV/dec to 122 mV/dec. It also exhibited a remarkable increase in the electrochemically active surface area, reaching 179 cm^2 compared to 22 cm^2 for NiS/NF. These improvements in surface area and kinetics contribute to its excellent stability, with the catalyst maintaining consistent performance over 20 h of continuous operation. These results underscore the effectiveness of the NiS-rGO-Ni/NF catalyst in methanol oxidation and its potential for more efficient and stable electrochemical applications.

1. Introduction

The global energy challenge has become increasingly urgent due to rising energy demand, driven by population growth and the widespread use of transportation, electronic devices, and computers. Traditionally, fossil fuels have been the primary energy source. However, their finite supply and the environmental damage they cause [1,2], particularly through greenhouse gas emissions, have prompted the search for sustainable alternatives [3]. Among these alternatives, hydrogen has gained attention for its clean energy potential. It offers high gravimetric energy density and produces zero emissions when used in fuel cells [4]. Despite its promise, hydrogen presents significant challenges. Its storage and transport are complicated by safety concerns, particularly its high flammability, which raises risk of leakage and explosions. These limitations hinder hydrogen's large-scale deployment, prompting the need for safer, more practical alternatives in energy systems. Methanol, by contrast, has emerged as a promising alternative [5]. Unlike hydrogen, it is liquid at room temperature, making storage and transport more manageable and less hazardous. Furthermore, methanol can be produced from renewable resources, such as captured CO_2, leading to the development of "*green methanol*". This aligns with global goals of carbon neutrality while offering a practical fuel option for a variety of

* Corresponding author.
** Corresponding author.
E-mail addresses: elmehdi.salmi@zoho.com (M. Salmi), SANAE.ELGHACHTOULI@univh2c.ma (S. El Ghachtouli).

https://doi.org/10.1016/j.ijhydene.2024.12.285
Received 18 August 2024; Received in revised form 29 November 2024; Accepted 16 December 2024
Available online 24 December 2024

applications. Direct methanol fuel cells (DFMCs) present a particularly attractive solution, capable of powering everything from portable electronics to electric vehicles, while also contributing to reduced carbon emissions [6–8].

The DMFC, known for its low pollutant emissions, high conversion efficiency, and impressive energy density, presents a viable option for powering electric vehicles and portable electronic devices [9]. In DMFC, methanol serves as the fuel at anode, undergoing methanol oxidation reaction (MOR), while oxygen (usually from air) is utilized at the cathode through oxygen reduction reaction (ORR) [10]. One of the primary challenges limiting the performance of DMFCs is the sluggish electron transfer kinetics of the methanol oxidation reaction (MOR) at the anode [11,12]. The slow reaction rates not only reduce the overall efficiency of the fuel cell but also lead to the accumulation of intermediate species, such as carbon monoxide (CO), which can poison the catalyst and further decrease its activity. Traditionally, precious metal-based catalyst, particularly platinum (Pt) and its alloys, have been used to accelerate MOR kinetics due to their excellent catalytic activity. However, the high cost of platinum, combined with its susceptibility to CO poisoning, has restricted its widespread use in large-scale DMFC applications [13]. This has prompted researchers to seek more cost-effective and robust alternatives [14]. Transition metal-based electrocatalysts, especially nickel-based chalcogenides [15–17] like nickel sulfides, have emerged as promising candidates [18–20]. Nickel sulfides offer comparable catalytic activity in alkaline media due to their favourable redox properties (Ni^{2+}/Ni^{3+}) and are far more affordable than platinum-based catalysts. Furthermore, nickel-based catalysts are known for their resistance to CO poisoning, which enhances their-long term stability and makes them suitable for use in DMFCs [21–23]. While nickel sulfide exhibit promising catalytic activity for the methanol oxidation reaction, their performance can be further enhanced by addressing their inherent limitations, such as low electrical conductivity and limited active surface area [24,25]. One effective strategy to overcome these challenges is the development of hybrid structures that incorporate conductive carbon materials like reduced graphene oxide (rGO), carbon nanotubes (CNTs), or carbon nanofibers (CNFs) [26–28]. These materials not only improve the overall conductivity of the electrocatalysts but also provide additional active sites for the methanol oxidation reaction, thereby enhancing the catalytic efficiency.

However, the structural design of the electrocatalysts is equally important in optimizing its performance. A high surface area is crucial for maximizing the exposure of active sites and facilitating efficient mass transport. This is where the dynamic hydrogen bubble template (DHBT) method plays a significant role. The DHBT method is a powerful technique for creating porous structures with high surface areas [29–31]. This method leverages the dynamic interplay of hydrogen evolution during electrochemical deposition to generate a unique porous morphology on the electrode surface. The principle of DHBT is based on the use of hydrogen bubbles formed during electrolysis as a template to introduce porosity into the deposited material. As the electrode material is deposited, hydrogen bubbles evolve at the electrode surface due to the electrochemical reduction of protons or water according to reactions (1) and (2). These bubbles act as physical spacers, preventing the deposition of material in certain areas and thus creating a porous network.

$$2H_2O + 2e^- \rightarrow H_2 + 2OH^- \quad (1)$$

$$2H^+ + 2e^- \rightarrow H_2 \quad (2)$$

The importance of the DHBT method lies in its ability to produce electrodes with high surface areas and enhanced catalytic performance [32–34]. The porous structure not only increases the active surface area but also facilitates better mass transport and diffusion of reactants, which are crucial for efficient electrocatalytic reactions. Additionally, this structure aids in the effective removal of reaction products, minimizing the risk of catalyst deactivation due to product accumulation, further contributing to the long-term stability and efficiency of the catalyst. The primary benefits of this method include its simplicity, cost-effectiveness, easy control of structures, and the ability to conduct the entire synthesis in short periods (e.g., 60s).

In this research, we focused on developing an electrode material based on nickel sulfide with an increased surface area to enhance the performance of the methanol oxidation reaction. Rather than directly depositing nickel sulfide onto a nickel foam substrate, we employed a two-step approach. First, a three-dimensional porous nickel layer was created using the dynamic hydrogen bubble template method. Next, reduced graphene oxide was electrodeposited to improve the electrode's electrical conductivity and serve as an anchor for nickel sulfide (denoted as NiS-rGO-Ni/NF). X-ray diffraction, X-ray photoelectron spectroscopy, and scanning electron microscopy analyses confirm the presence of Ni_3S_2 and Ni_3S_4 phases in a highly porous structure. Cyclic voltammetry revealed significantly better performance compared to NiS/NF, with a lower onset potential for Ni^{3+} formation and a 20-fold increase in its surface concentration. Electrochemical impedance spectroscopy revealed efficient electron transfer, indicated by significantly reduced charge transfer resistance. Methanol electrooxidation experiments showed that the NiS-rGO-Ni/NF electrode achieved higher current densities and lower Tafel slope compared to NiS/NF. The integration of reduced graphene oxide and porous nickel bolstered electrocatalytic performance. Stability testing over 20 h affirmed durability. Density functional theory (DFT) calculations were used to explore the catalytic activity of methanol oxidation on nickel sulfide surfaces. Gibbs free energy diagrams revealed several spontaneous pathways for converting CH_3OH to CO_2, emphasizing the role of nickel sulfide surfaces in facilitating methanol oxidation reactions (MOR). These theoretical insights offered a deeper understanding of the reaction mechanisms and supported the experimental findings. In conclusion, the electrode shows potential for effective methanol electrooxidation and provides valuable insights for catalyst optimization.

2. Experimental

2.1. Reagent

Graphite, sodium nitrate ($NaNO_3$), potassium permanganate ($KMnO_4$), hydrogen peroxide (H_2O_2, 35%), sulfuric acid (H_2SO_4, 98%), hydrochloric acid (HCl, 37%), nickel chloride hexahydrate ($NiCl_2.6H_2O$), thiourea ($SC(NH_2)_2$), potassium hydroxide (KOH), sodium chloride (NaCl), ammonium chloride (NH_4Cl), potassium dihydrogen phosphate (KH_2PO_4), dipotassium hydrogen orthophosphate (K_2HPO_4), and methanol (CH_3OH, 99%) were purchased from Sigma-Aldrich and were used as received without further purification. All solutions were prepared using deionized water from the Milli-Q system.

2.2. Electrochemical measurements

All electrochemical experiments were performed with an Autolab electrochemical workstation (PGSTAT128 N, Metrohm) controlled by a computer with NOVA 2.1.5 software. A conventional three-electrode system was used, with nickel foam (NF, dimensions: 5 mm × 10 mm x 0.3 mm, surface area: 0.7 cm^2) as working electrode, a platinum plate as the counter electrode, and $Ag/AgCl_{(Sat)}$ as the reference electrode. Prior to each experiment, the nickel foam was cleaned using HCl (3 M), acetone, ethanol, and deionized water in an ultrasonic bath for 10 min each [35]. Then, the electrode was dried at room temperature and properly stored for future use. All measurements were performed under ambient conditions. The recorded current densities are expressed in terms of geometric surface area, with no IR-drop correction.

2.3. Preparation

2.3.1. Preparation of three dimensional (3D) porous nickel (Ni/NF)

The nickel foam (NF) substrate was initially treated with a

hydrochloric acid (3 M) solution to remove surface oxide layers. Subsequent cleaning involved rinsing with deionized (DI) water and ethanol. A three-dimensional porous nickel layer was prepared using a dynamic hydrogen bubble template-assisted [29] electrodeposition method on nickel foam (NF). The plating bath, with a volume of 50 mL and a pH of 4, consisted of 0.1 M nickel chloride hexahydrate ($NiCl_2.6H_2O$), 1 M ammonium chloride (NH_4Cl), and 1 M sodium chloride (NaCl) [32]. Employing galvanostatic electrodeposition, a three-electrode setup was utilized, with the cleaned nickel foam (0.7 cm^2 active surface area) serving as the working electrode. The deposition of the porous nickel layer was achieved by applying a controlled current density of -0.35 A cm^{-2} for 60 s. Following deposition, the electrode underwent multiple DI water rinses to remove residual electrolyte solution from the pores. Subsequently, the electrode was air-dried at room temperature, resulting in the formation of the desired three-dimensional porous nickel layer on the nickel foam substrate designated Ni/NF electrode.

2.3.2. Preparation of reduced graphene oxide supported on 3D porous Ni/NF (rGO-Ni/NF)

Graphene oxide (GO) was first synthesized from natural graphite powder through a modified Hummer's method [36]. The electrochemical deposition process for the GO film onto the Ni/NF surface was performed following the method detailed by Z. Yong et al. [37]. For electrolyte preparation, 50 mg of GO was dispersed in 50 mL of 0.2 M phosphate buffer solution (pH = 4) using ultrasonic treatment for 1 h. For the electrochemical experiments, a conventional three-electrode cell configuration was adopted, including the previously prepared Ni/NF as working electrode. Cyclic voltammetry was performed by sweeping the potential in the range of 0 to -1.3 V at a scan rate of 50 mV s^{-1} for 50 cycles. Following the cyclic voltammetry measurements, the resulting rGO-Ni/NF electrode was carefully removed, thoroughly rinse with DI water, dried, and subsequently store for further analysis.

2.3.3. Preparation of nickel sulfide decorated rGO-Ni/NF (NiS-rGO-Ni/NF)

Nickel sulfide was electrodeposited onto the rGO-Ni/NF electrode using a potentiodynamic method. The electrodeposition process took place in a 50 mL aqueous solution containing 5.0 mM $NiCl_2.6H_2O$ and 100 mM thiourea at a pH of 6.5. Cyclic voltammetry was employed to achieve this, with the potential scanned between -1.0 V and 0.2 V vs Ag/AgCl for 20 cycles with a scan rate of 20 mV s^{-1}. Following the electrodeposition, the NiS-rGO-Ni/NF electrode was carefully removed from the deposition bath and thoroughly rinsed with abundant DI water. Subsequently, it was dried at room temperature and securely stored for further characterization and subsequent electrochemical experiments. For comparison, NiS/NF was also prepared using the same procedure without the incorporation of the porous nickel layer and graphene oxide. Throughout the manuscript, we will refer to the electrode material as NiS-rGO-Ni/NF for simplicity, which comprises nickel sulfide, reduced graphene oxide, and a porous nickel layer.

2.4. Characterization

The morphology of electrodeposited nickel sulfide was determined using Zeiss Evo 10 SEM with a SmartEDX detector, using an accelerating voltage of 10 keV. The crystal phases of the samples were determined using the XRD diffractometer Bruker D8 Advance, equipped with a Lynx-Eye detector, a graphite monochromator, and parallel beam optics with Cu radiation Kα (λ_{Cu} = 1.541 Å). X-ray photoelectron spectroscopy (XPS) spectra were recorded by a XPS KRATOS, AXIS $Ultra^{DLD}$ spectrometer with the monochromatized Al-Kα X-ray source (hν = 1486.6 eV) and an X-ray beam of around 1 mm. The analyser was operated in constant pass energy of 40 eV using an analysis area of approximately 700 μm × 300 μm. CasaXPS software was used for all data processing. The XPS experiment and data treatment were made according to the same procedures previously described [38].

2.5. Computational details

First-principles density functional theory (DFT) calculations were performed using the Vienna Ab-initio Simulation Package (VASP) with the projector augmented wave (PAW) method to model electron-core interactions [39–42]. The exchange-correlation interactions were described using the generalized gradient approximation (GGA) with the Perdew-Burke-Ernzerhof (PBE) functional [43]. A plane wave basis set was employed with a kinetic energy cutoff of 450 eV. To ensure higher accuracy in evaluation the adsorption of CH3OH and other intermediate molecules, additional simulations were conducted with a 520 eV energy cutoff and a k-point mesh of 3 x 2 x 1 for Ni_3S_2 and 2 x 3 x 1 for Ni_3S_4. Geometry optimizations were performed until the total energy convergence was below 1×10^{-5} eV and the force per atom was less than 0.02 eV $Å^{-1}$. Both the (101) and (001) slabs were modelled, exposing the (101) surface for Ni_3S_2 with a 4 x 2 $\sqrt{3}$ supercell and the (001) surface for Ni_3S_4 with a 3 x 1 supercell, cleaved from the bulk Ni_3S_x, materials, and separated by a vacuum layer of approximately 10 Å. The bottom two layers of the slabs were fixed in their bulk positions, while the upper layers and adsorbate molecules were allowed to optimize fully. The open-source package vaspkit [44] was used for the state of density and the thermodynamics (298.51 K and 1 atm) calculations.

3. Results and discussion

3.1. Synthesis

The fabrication process of the NiS-rGO-Ni/NF electrode involved a sequence of three distinct steps, as depicted in Fig. 1. First, a porous layer of Ni was constructed on nickel foam substrate through a process involving template electrodeposition facilitated by hydrogen bubble evolution. This phenomenon occurs when a high cathodic current density (-0.35 A cm^{-2}) is applied to the electrode. This high negative current density essentially creates an environment where electrons are readily available. At the interface between the nickel foam substrate and the aqueous electrolyte, two key reactions take place (reaction 3 and 4):

$$2H^+ + 2e^- \rightarrow H_{2\,(g)} \tag{3}$$

$$2NH_4^+ + 2e^- \rightarrow NH_{3(g)} + H_{2\,(g)} \tag{4}$$

These reactions generate hydrogen gas (H_2) bubbles. These bubbles act as a template, leaving voids behind as they rise from the electrode surface. Simultaneously, another reaction occurs (reaction 5):

$$2Ni^{2+} + 2e^- \rightarrow Ni_{(s)} \tag{5}$$

This reaction involves the reduction of nickel ions (Ni^{2+}) in the solution by the electrons available at the cathode. This reduction process deposits nickel metal atoms (Ni) onto the surface of the NF substrate. However, the presence of hydrogen bubbles plays a key role. The growth of Ni atoms only occurs in the areas where no bubbles are formed. This selective deposition ultimately gives rise to a distinctive porous structure (Fig. 1.1). As the electrochemical reactions progress, this interconnected porous structure becomes integrated with the underlying NF substrate. This innovative approach results in a highly engineered porous Ni/NF structure, forming the initial foundation of the NiS-rGO-Ni/NF electrode.

Second, potentiodynamic deposition method proved effective in facilitating the direct electrodeposition of graphene oxide (Fig. 1.2). It is worth noting that the chemical reduction of GO in aqueous solution often leads to irreversible agglomeration [45] (due to insolubility of reduced graphene oxide). Thus, a logical inference can be made that when GO comes into direct contact with the electrode surface and accepts electron (electrochemical reduction), the resultant graphene oxide

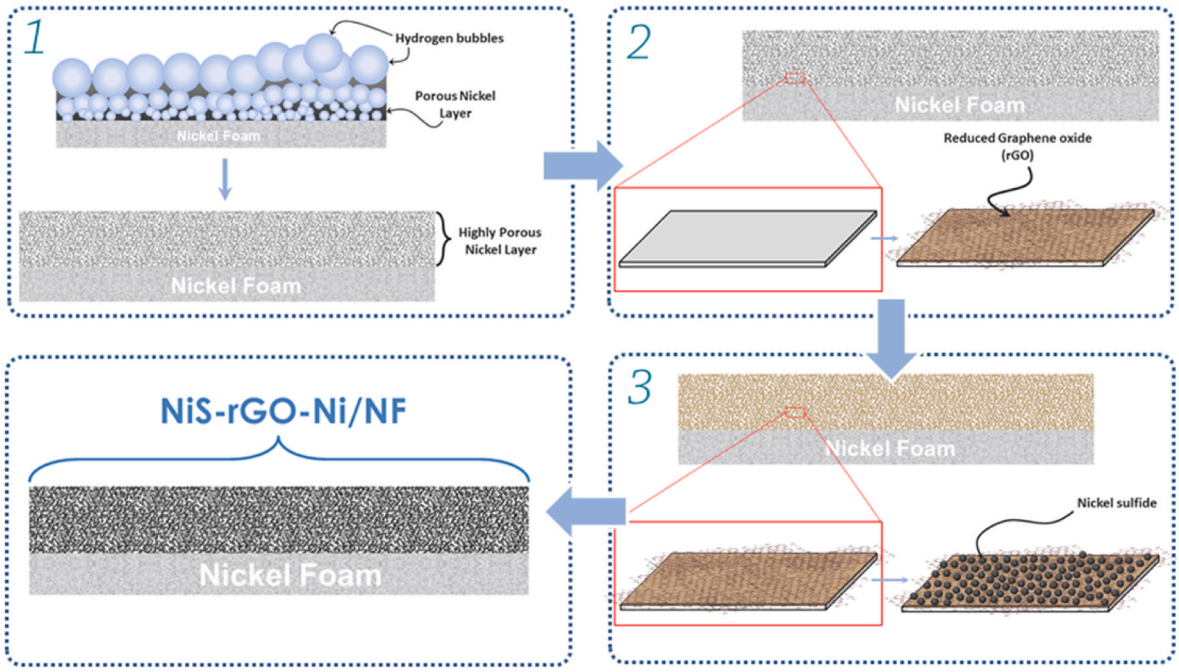

Fig. 1. Schematic diagram of the NiS-rGO-Ni/NF electrode preparation steps.

will similarly exhibit insolubility. This phenomenon, in turn, facilitates the direct adherence of the reduced graphene oxide onto the electrode surface. Fig. 2a shows the obtained cyclic voltammogram of GO electrodeposition on the prepared Ni/NF electrode. The progressive increase in peak current with each successive potential sweep clearly indicates the successful deposition of conductive graphene oxide onto the surface of the Ni/NF electrode from the GO suspension [46–48].

Finally, NiS grown on rGO-Ni/NF (Fig. 1.3) was synthesized using a facile potentiodynamic deposition (Fig. 2b) with the electrolyte consisting of $NiCl_2$ and Thiourea ($CS(NH_2)_2$). During the electrochemical process, the formation of NiS occurs as a result of various chemical and/or electrochemical reactions [49,50] (reaction 6 and 7) taking place in the deposition bath which can be summarized as follows. The reduction of water yields hydroxide ions, which subsequently engage with both thiourea and Ni^{2+} ions to generate a complex involving thiourea, Ni^{2+}, and hydroxide. This complex eventually decomposes, leading to the formation of nickel sulfide.

$$2H_2O + e^- \rightarrow 2OH^- + H_2 \quad (6)$$

$$Ni^{2+} + CS(NH_2)_2 + 2OH^- \rightarrow [Ni(OH)_2CS(NH_2)_2] \rightarrow NiS + H_2HCN + 2H_2O \quad (7)$$

3.2. Structural and morphological characterization

3.2.1. X-ray diffraction

The crystal structure and phase composition of the electrodeposited NiS-rGO-Ni/NF hybrid material were investigated using X-ray diffraction (XRD) measurements. The diffraction patterns are presented in the accompanying Fig. 3a. In the XRD spectrum of NiS-rGO-Ni/NF material, deposited onto NF substrate, distinct peaks are observed at 44.25°, 51.56°, and 76.14°, corresponding to (111), (200), and (220) crystallographic planes, respectively. These peaks primarily arise from the Ni foam substrate. Notably, there are no discernible peaks associated with nickel sulfide in the spectrum. The absence of peaks could be attributed to the possibly thin and disordered nature of the deposited film, coupled with the high intensity of peaks originating from Ni foam substrate, which may hinder the detection of new peaks [51,52].

The analysis of the initial layer in the hybrid material, comprising a porous nickel layer, involved scraping the deposit from the NF substrate and examining it in powder form. The XRD pattern exhibited identical peaks to those observed on the Ni foam itself. This unequivocally confirms that the first deposited porous layer is composed entirely of metallic nickel. Regarding the graphene oxide layer, no distinct peak

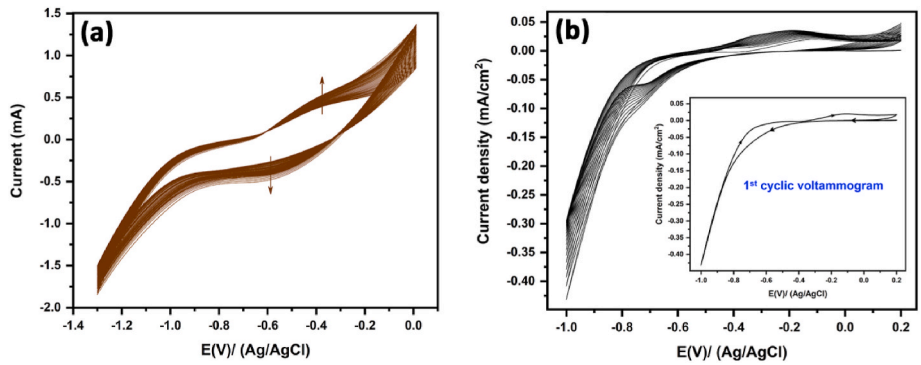

Fig. 2. (a) Cyclic voltammograms of the electrodeposition of graphene oxide (1 mg/ml GO in 0.2 M PBS solution). 50 CV cycles, at V = 50 mV s^{-1}. (b) Cyclic voltammograms of nickel sulfide electrodeposition on rGO-Ni/NF (500 mM of thiourea +5 mM $NiCl_2.6H_2O$), 15 CV cycles at V = 5 mV s^{-1}.

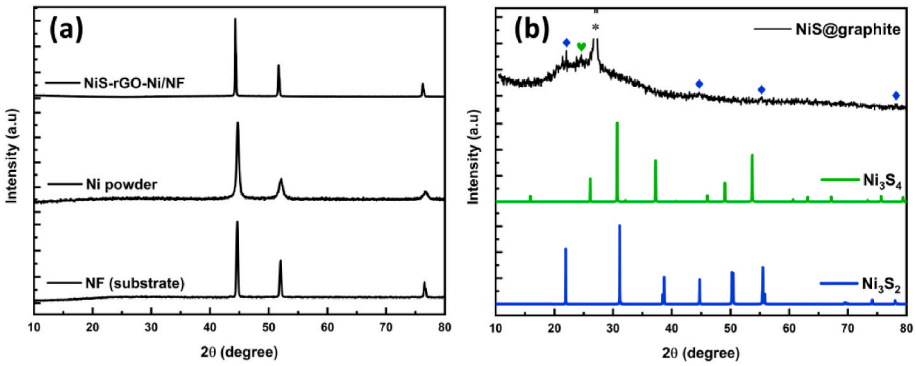

Fig. 3. (a) XRD pattern of the prepared materials on Ni foam. (b) XRD pattern of nickel sulfide electrodeposited on graphite substrate.

was observed despite an increase in the quantity of deposited graphene oxide. On the other hand, for the nickel sulfide layer, a modification was made by replacing Ni foam substrate with a graphite rod. The deposition process was conducted solely with the nickel sulfide layer, excluding the other layers, and involved a higher number of cycles during the potentiodynamic deposition. Fig. 3b displays the obtained diffractogram in which the diffraction peaks, highlighted in blue, can be attributed to the (101), (202), (122), and (223) planes of rhombohedral Ni_3S_2 (*JCPDS card no. 44–1418*). Additionally, the peak marked in green corresponds to the (220) plane of cubic Ni_3S_4 (*JCPDS card no. 47–1739*). However, the prominent diffraction peak marked by a black star, comes from the (111) plane of the graphite substrate (*JCPDS card no. 75–2078*).

3.2.2. Scanning electron microscopy

The scanning electron microscopy (SEM) analysis of the prepared materials, which includes a porous nickel layer, reduced graphene oxide, and nickel sulfide deposited on the NF substrates, reveals distinct morphologies for each layer. The SEM images (Fig. 4) illustrates the unique structural features of these components, offering detailed insights into the complex architecture of the hybrid NiS-rGO-Ni/NF material.

The NF substrate exhibits a smooth surface characterized by clearly discernible grain boundaries. The porous nickel layer deposited on the NF substrate (Ni/NF) stands out due to its highly porous dendritic structure. The porous nature of this layer is notably pronounced, with interconnected dendritic formations that create a network of voids and channels. The non-compact structure of the layer enhances its surface area. The deposition of reduced graphene oxide on Ni/NF results in a non-uniform carbonaceous layer, shown in Fig. S1. This layer exhibits a distinctive morphology characterized by a needle-like structure (Fig. 4). The nickel sulfide (NiS-rGO-Ni/NF), constituting the final layer, shares a similar morphology to the porous nickel but with filled spaces between the dendrites. Notably, there are no distinct nickel sulfide particles or thin layer observed. However, when comparing it with nickel sulfide directly deposited onto nickel foam (Fig. S2), changes in the substrate's surface become apparent. This is demonstrated by the emergence of new grain boundaries and the non-uniform distribution of small particles on the surface. Energy-dispersive X-ray (EDX) analysis (Fig. S3) further confirms the presence of nickel sulfide. The elemental mapping demonstrates the distribution of nickel and sulfur throughout the porous structure, validating the successful incorporation of nickel sulfide. These observations, derived from SEM imaging and EDX analysis, collectively elucidate the detailed morphological changes at each stage of material deposition. They emphasize how each layer contributes to the overall architecture of the hybrid material, enhancing its potential for catalytic applications.

3.2.3. XPS

X-ray photoelectron spectroscopy (XPS) was employed to analyse the chemical composition and oxidation states of the elements presents in

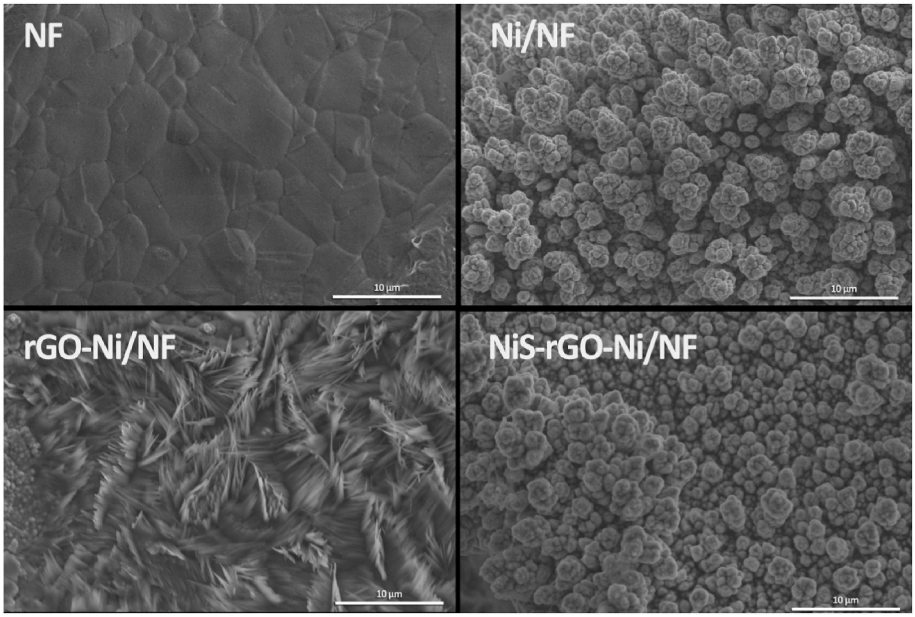

Fig. 4. SEM images of the prepared material at different stages.

the NiS-rGO-Ni/NF electrode, providing valuable insights into how these features contributes to the enhanced catalytic activity. The survey scans (Fig. S4) confirmed the presence of nickel (Ni), oxygen (O), carbon (C), and sulfur (S), all of which play critical roles in the electrochemical performance of the electrodes. High-resolution XPS (Figs. S5 and S6) provided further insights into the chemical states of these elements, offering explanations for the observed improvements in activity.

The Ni 2p spectrum (Fig. S5) revealed distinct peaks at approximately 855 eV and 873 eV, corresponding to Ni^{2+}, confirming the presence of nickel sulfide. Nickel sulfide's redox pair (Ni^{2+}/Ni^{3+}) is crucial for promoting the methanol oxidation reaction (MOR), as Ni^{2+} is readily oxidized to Ni^{3+} during the reaction, enhancing catalytic efficiency. Additionally, a peak at around 852.5 eV corresponds to metallic nickel (Ni^0), indicating the presence of some unreacted nickel species. The presence of metallic nickel may further improve electrical conductivity, facilitating faster electron transfer during MOR. Interestingly, the peak observed at 856.1 eV is assigned to Ni^{3+}, which suggests partial surface oxidation of nickel sulfide, contributing to the formation of an active Ni^{3+} species that is known to enhance MOR kinetics by accelerating the oxidation of methanol. The S 2p spectrum (Fig. S6) provided further confirmation of nickel sulfide, with a peak at 163.1 eV corresponding to S^{2-} in the Ni–S bond. The integrity of the Ni–S is crucial for the electrochemical activity of the material, as the sulfur atoms help stabilize the nickel centers and facilitate electron transfer. Another peak at 168.7 eV corresponds to oxidized sulfur species, possibly in the form of sulfate (SO_4^{2-}) or sulfite ($S_2O_3^{2-}$) ions [53–55]. While these oxidized sulfur species may result from surface oxidation, their presence could also contribute to enhanced catalytic activity by introducing additional active sites or promoting charge transfer at the electrode-electrolyte interface. The C 1s spectrum provided key insights into the reduced graphene oxide (rGO) component of the electrode. A peak at around 284.5 eV is associated with sp3 hybridized carbon atoms, confirming the presence of graphene sheets within the composite. The high electrical conductivity of rGO plays a vital role in improving the overall electron transfer within the catalyst, thereby enhancing its catalytic performance. Additonally, peaks at 286.6 eV and 288.5 eV indicate the presence of oxygen-containing functional groups, such as C–O and C=O bonds. These functional groups on rGO not only help anchor nickel sulfide nanoparticles but may also promote electron mobility across the catalyst surface, further contributing to the improved electrochemical performance of the electrode. The O 1s spectrum (Fig. S5) revealed the presence of oxygen species within the electrode. A prominent peak at 529.6 eV is attributed to oxygen bonded to nickel, likely in the form of nickel oxide (NiO) or nickel hydroxide ($Ni(OH)_2$) [56]. These species can form thin surface layers that enhance the oxidation process during MOR by providing additional reaction sites. The peak at 533.4 eV is associated with adsorbed water molecules on the electrode surface [57], which might affect the electrode's surface chemistry, potentially facilitating the methanol oxidation process by enhancing proton mobility. Overall, the XPS analysis provides strong evidence of the successful deposition of nickel, nickel sulfide, and reduced graphene oxide on the nickel foam substrate. The presence of Ni^{2+} and Ni^{3+} species, along with the well-integrated rGO, plays a pivotal role in enhancing the catalytic activity of the NiS-rGO-Ni/NF electrode. Specifically, the Ni^{2+}/Ni^{3+} redox pair actively participates in the methanol oxidation reaction, while the rGO significantly improves electrical conductivity, facilitating rapid electron transfer.

3.2.4. Electrochemical behaviour of the electrode in 1 M KOH solution

To assess the electrochemical performance of the NiS-rGO-Ni/NF hybrid electrode, we carried out a comprehensive comparative electrochemical analysis against control samples. These control samples included the rGO-Ni/NF electrode without nickel sulfide, the Ni/NF electrode devoid of both reduced graphene oxide and nickel sulfide, and finally, the NiS/NF electrode consisting of nickel sulfide growth on nickel foam substrate. This comparative approach allowed us to systematically explore and contrast the specific contributions of each component in the NiS-rGO-Ni/NF hybrid electrode.

As can be seen in Fig. 5a, all electrodes exhibited prominent redox peaks. These peaks originate from the faradaic reactions between Ni^{2+} on the electrode surface and OH^- ions from the electrolyte [58–60]. The corresponding reversible reactions can be described by the following equations:

$$Ni + 2OH^- \rightarrow Ni(OH)_2 + 2e^- \quad (8)$$

$$Ni(OH)_2 + OH^- \rightarrow NiOOH + H_2O + e^- \quad (9)$$

$$NiS + OH^- \rightarrow NiS(OH) + e^- \quad (10)$$

It is important to note that prior to conducting the electrochemical tests, a series of 10 consecutive potential sweeps ranging from 0 to 0.6 V were performed in a 1 M KOH solution at a potential scan rate of 10 mV s^{-1}. This process was employed not only to establish a consistent and stable cyclic voltammogram response but also to effectively activate the electrode, a practice substantiated by previous studies [61–64]. During this continuous potential scanning, any metallic nickel on the surface undergoes oxidation, forming α-$Ni(OH)_2$ according to reaction (8) [65]. The oxidation peak associated with this transformation is visible in the first cyclic voltammogram of the electrodes when immersed in the KOH solution (Fig. S7).

As depicted in Fig. 5a, the NiS-rGO-Ni/NF hybrid electrode demonstrates superior electrochemical performance in comparison to the other electrodes. This is evidenced by its significantly higher oxidation and reduction peak current densities, as well as the larger peak area. These features indicate the presence of numerous electroactive species and active sites on the NiS-rGO-Ni/NF electrode. In addition, the onset potential of Ni^{2+} oxidation for both NiS-rGO-Ni/NF and NiS/NF catalysts is displayed in Fig. 5b. As shown in the figure, the curves highlight the enhanced electrochemical performance achieved with the NiS-rGO-Ni/NF catalyst. By integrating reduced graphene oxide (rGO) and porous nickel layer into the NiS/NF structure, the NiS-rGO-Ni/NF electrode achieves a notably reduced onset potential of 328 mV. This represents a substantial enhancement over the 359 mV observed for the NiS/NF electrode, resulting in a notable difference of 31 mV.

The effect of the potential scan rate can provide insights into the mechanism governing the redox process, whether it is surface-limited or diffusion-controlled [66]. As shown in Fig. 8c, the cyclic voltammetry curves of the NiS-rGO-Ni/NF electrode, recorded in a 1 M KOH solution at scan rate ranging from 5 to 60 mV s^{-1}, reveal key trends. Notably, both the anodic and cathodic peak current densities increased with the scan rate. Additionally, the oxidation and reduction peak positions shifted in opposite directions, a typical characteristic of a quasi-reversible redox process. To determine whether the redox process is diffusion-controlled or capacitive, we examined the slope of the linear relationship between Log(i) and Log(υ) using to the following equations:

$$i = a\nu^b \quad (11)$$

$$Log(i) = Log(a) + bLog(\nu) \quad (12)$$

Here, υ represents the scan rate, and $\boldsymbol{a}$ and $\boldsymbol{b}$ are adjustable parameters. Typically, when $\boldsymbol{b} = 1$, it suggests a capacitive process, whereas $\boldsymbol{b} = 0.5$ indicates an ideal diffusion-controlled Faradaic process [67,68]. In this case, the slope was approximately 0.51 (Fig. S8), which closely aligns with the anticipated value of 0.5 for a process that's controlled by diffusion. Consequently, these results strongly suggest that the diffusion of OH^- ions is the rate-limiting step of the Ni^{2+}/Ni^{3+} redox process.

Additional valuable information can be extracted from the analysis of the evolution of peak current in relation to the scan rate, specifically regarding the surface concentration of the Ni^{2+}/Ni^{3+} redox species. This concentration can be determined using the following equation [69,70]:

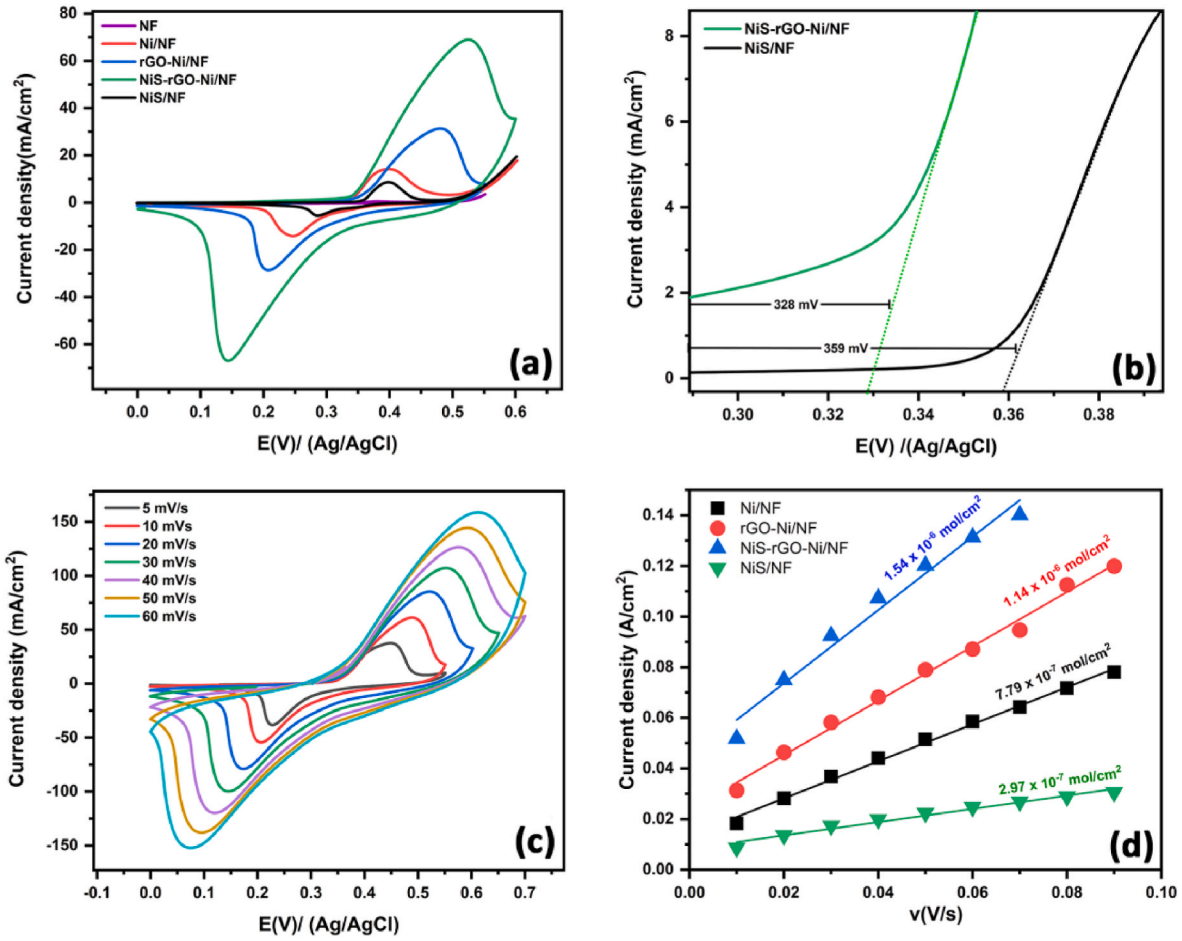

Fig. 5. (a) Cyclic voltammograms of the electrodes in 1 M KOH solution at a potential scan rate of 10 mV s^{-1}. (b) Linear sweep voltammetry of NiS/NF and NiS-rGO-Ni/NF in 1 M KOH solution at a potential scan rate of 10 mV s^{-1}. (c) Cyclic voltammograms of NiS-rGO-Ni/NF electrode at various scan rate (5–60 mV s^{-1}). (d) Surface coverage of Ni^{2+} on the prepared electrodes.

$$Ip = \left(\frac{n^2F^2A\Gamma}{4RT}\right)v \tag{13}$$

Here, Ip represents the peak current (A), n signifies the number of electron transferred, R is the universal gas constant (8.314 J mol^{-1} K^{-1}), T denotes the temperature (298.15 K), F stands for the Faraday's constant (96485.44 s A mol^{-1}), A corresponds to the geometric surface area (cm^2), v represents the potential scan rate ($V.s^{-1}$), and Γ represents the surface concentration of the redox species ($mol.cm^{-2}$). By analysing the relationship between Ip and v, the surface concentration of the electrodes was derived, as depicted in Fig. 5d. Notably, the surface concentration witnessed a substantial increase by a factor close to 20, going from 1.54 × 10^{-7} mol cm^{-2} for NiS/NF electrode to 29.7 × 10^{-7} mol cm^{-2} for NiS-rGO-Ni/NF electrode. This notable augmentation finds its explanation in the integration of rGO and porous Ni layer onto the nickel foam substrate, consequently providing more surface area, allowing for a greater number of electroactive species.

The double layer capacitance (C_{dl}), essential for determining the electrochemically active surface area (ECSA), was evaluated through cyclic voltammetry within the capacitive region (−0.10 – 0.10 V vs Ag/AgCl) at various scan rates ranging from 10 to 60 mV s^{-1}. To derive C_{dl}, the average capacitive current Δi was calculated using the formula $\Delta i = |i_c - i_a|/2$, where i_c represents the cathodic current and i_a is the anodic current, recorded at 0 V vs Ag/AgCl. The resulting Δi values were plotted against different scan rates, and the linear slope obtained corresponded to the value of C_{dl}. The ECSA was then estimated using to relationship ECSA = C_{dl}/C_s, where C_s is a known constant with the value of 0.04 mF cm^{-2}.

As depicted in Fig. S9, the double layer capacitance of the NiS-rGO-Ni/NF hybrid electrode (7.16 mF) significantly surpasses that of the NiS/NF electrode (0.88 mF), indicating a notable difference in the electrochemically active surface area (22 cm^2 for NiS/NF and 179 cm^2 for NiS-rGO-Ni/NF). This contrast can be attributed to a substantial enhancement in surface roughness achieved through the incorporation of a porous nickel layer using DHBT deposition and also the integration of graphene oxide, as illustrated in the SEM images. Notably, the NiS-rGO-Ni/NF hybrid electrode exhibits the highest ECSA value (179 cm^2), followed by rGO-Ni/NF (61.75 cm^2), Ni/NF (48.75 cm^2), and NiS/NF (22 cm^2). This trend aligns with the observed surface coverage of the redox active species.

3.2.5. *Electrochemical impedance spectroscopy*

To gain insights into the enhanced electrochemical performance of the NiS-rGO-Ni/NF hybrid electrode, electrochemical impedance spectroscopy (EIS) was performed over a frequency range from 100 kHz to 10 mHz at open circuit potential (OCP) in a 1 M KOH solution. The obtained results are illustrated in Fig. 6a. The data were further analysed using *Zview* software, and the corresponding fitted parameters, as outlined in Table 1, were derived from simulations based on equivalent circuits 1 and 2, as depicted in Fig. 6b. The Nyquist plots for Ni/NF, rGO-Ni/NF, and NiS/NF show identical patterns, each consisting of two semicircles. The high-frequency semicircle is associated with the internal resistance of the electrode, which includes the ionic resistance of the electrolyte, the intrinsic resistance of the active material, and the

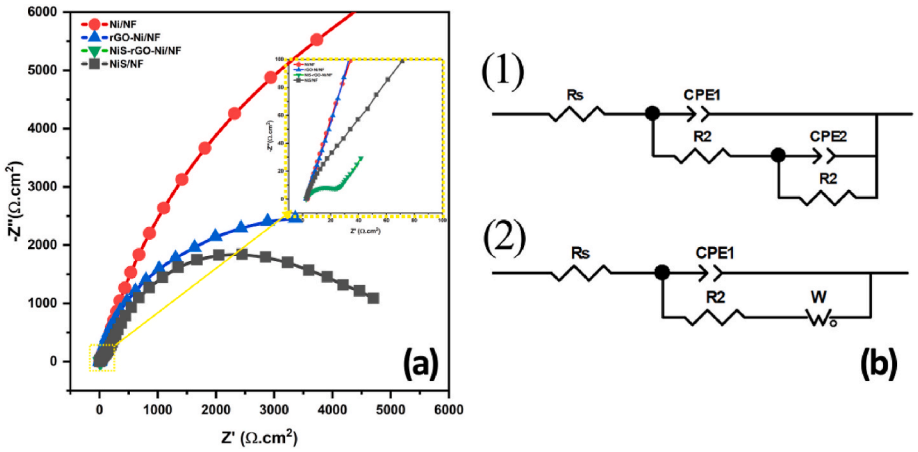

Fig. 6. (a) Nyquist plots of the prepared electrodes in 1 M KOH solution at open circuit potential (−0.15 V vs Ag/AgCl. (b) Equivalent circuits used to simulate the EIS data.

Table 1
Extracted parameter values from the EIS data fitting.

Electrode	R_s (Ω.cm^2)	R_1 (Ω.cm^2)	CPE_1		R_2 (Ω.cm^2)	CPE_2		W (σ) (Ω.S$^{-1/2}$)	χ^2
			$Q.10^4$(Ω^{-1}.S^{n}cm^{-2})	n		$Q.10^4$(Ω^{-1}.S^n.cm^{-2})	n		
Ni/NF	3.28	56.84	37.67	0.85	18538	11.12	0.85	–	5.95×10^{-5}
GO-Ni/NF	2.33	10.31	73.94	0.78	5651	15.50	0.87	–	19.29×10^{-5}
NiS-rGO-Ni/NF	2.45	–	–	–	25.47	1079.4	0.69	139.8	15.55×10^{-5}
NiS/NF	2.52	116.6	3.99	0.77	4830	6.01	0.85	–	85.37×10^{-5}

contact resistance between the active material and the nickel foam substrate. Meanwhile, the low-frequency semicircle is attributed to the charge transfer resistance (R_2) at the electrode/electrolyte interface. In contrast, the NiS-rGO-Ni/NF electrode exhibited a markedly different Nyquist plot. Notably, the high-frequency semicircle, indicative of internal resistance, was absent, implying a substantially lower internal resistance compared to the other electrodes. Instead, a nearly vertical line was observed in the low-frequency region, suggesting that the rate-limiting step for the NiS-rGO-Ni/NF electrode is governed by diffusion-controlled processes rather than charge transfer. This straight line is indicative of Warburg impedance, which signifies diffusion limitations of hydroxide ions (OH^-) in the electrolyte, particularly during the Ni^{2+} to Ni^{3+} conversion.

The NiS-rGO-Ni/NF electrode exhibited the most efficient electron transfer for Ni^{2+} to Ni^{3+} conversion, as evidenced by its lowest charge transfer resistance (R_2) value. This observation, detailed in Table 3, highlights the enhanced conductivity and efficiency of the NiS-rGO-Ni/NF hybrid electrode in facilitating the redox reactions involved in methanol electrooxidation. The reduced R_2 value indicates a lower resistance to charge transfer at the electrode/electrolyte interface, contributing to its superior electrocatalytic performance.

3.2.6. *Electrooxidation of methanol in 1 M KOH solution*

To showcase the benefit arising from the incorporation of rGO and the porous Ni layer onto NiS/NF electrode, methanol electrooxidation was carried out. This study took place in a 1 M KOH solution containing 0.1 M CH_3OH in order to evaluate the efficacy of the NiS-rGO-Ni/NF hybrid electrode. For the purpose of comparison, a series of other electrode configuration were also examined, including NF substrate, Ni/NF, rGO-Ni/NF, and NiS/NF (Fig. 7).

As can be seen from Fig. 7a, all electrodes exhibit distinct catalytic activity with regards to methanol electrooxidation. It is evident that the NiS-rGO-Ni/NF hybrid electrode exhibits the most pronounced catalytic performance, attaining a notably higher current density of 84.10 mA cm^{-2} at 0.55 V. This performance surpasses that of the other electrodes configurations, namely rGO-Ni/NF (56.82 mA cm^{-2}), Ni/NF (34.21 mA

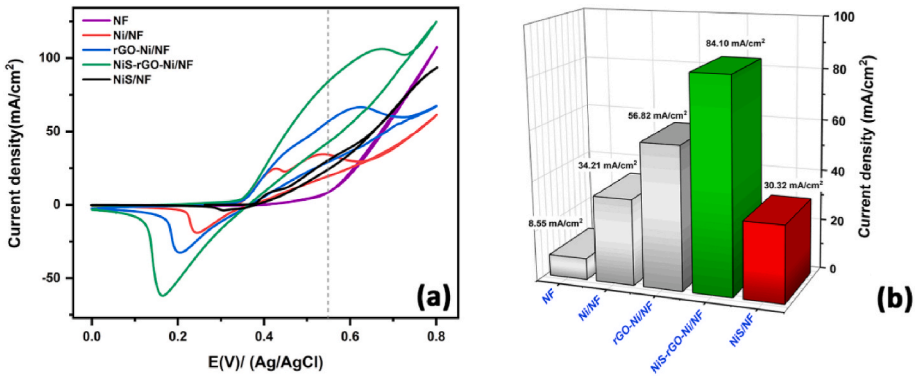

Fig. 7. (a) Cyclic voltammograms of the electrodes in 1 M KOH solution in the presence of 0.1 M of methanol (scan rate: 10 mV s^{-1}). (b) Current densities of methanol oxidation collected at 0.55 V vs Ag/AgCl.

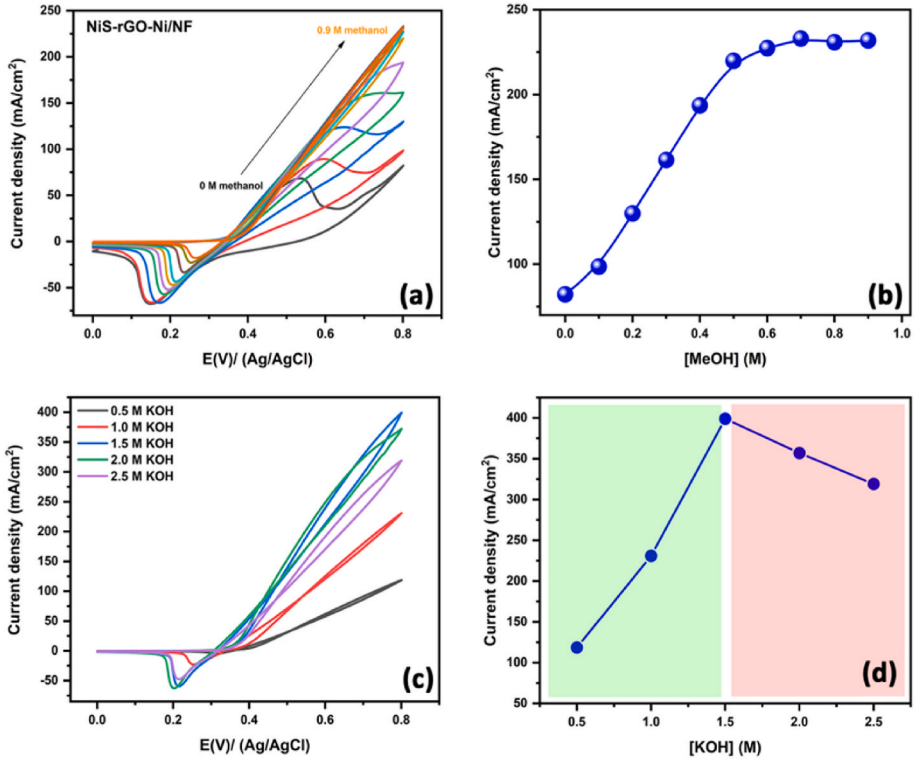

Fig. 8. (a) Cyclic Voltammograms of NiS-rGO-Ni/NF hybrid Electrode in 1.0 M KOH Solution with different Methanol Concentrations (0.1–0.9 M) at a Scan Rate of 10 mV s^{-1}. (b) Methanol concentration dependency on the current density of methanol electrooxidation. (c) Cyclic voltammograms of NiS-rGO-Ni/NF hybrid electrode in the presence of 0.5 M methanol at varied KOH concentration. (d) Dependency of KOH concentration on the current density of methanol electrooxidation.

cm^{-2}), NF (8.55 mA cm^{-2}), and stands approximately 2.7 times higher than that of the NiS/NF electrode (30.32 mA cm^{-2}), as depicted in Fig. 7b. In addition, the Tafel slopes derived from methanol electrooxidation experiments using NiS/NF (122 mV.dec^{-1}) and NiS-rGO-Ni/NF (204 mV.dec^{-1}) electrodes, as depicted in Fig. S10, highlight the superior electrocatalytic efficacy of the latter configuration. The decrease in Tafel slope in the NiS-rGO-Ni/NF hybrid electrode signifies enhanced reaction kinetics and a notable improvement in catalytic performance during methanol electrooxidation. This improvement highlights the stronger ability of the NiS-rGO-Ni/NF hybrid electrode in catalysing methanol oxidation. This enhanced performance is primarily due to the combined effect of reduced graphene oxide, which provides good electronic conductivity (indicated by a decrease in charge transfer resistance from 4830 to 25.47 Ω cm^2), and porous nickel, which increases the electrode's available surface area (expanding from 22 to 179 cm^2). This combination has proven to be advantageous in dispersing the active component, leading to better electrocatalytic performances.

The electrocatalytic oxidation of methanol is governed by a complex interplay of factors that collectively define its efficiency. These factors include catalyst loading, KOH concentration, and the concentration of methanol itself, each playing a crucial role in shaping the performance of the NiS-rGO-Ni/NF hybrid electrode toward methanol electrooxidation. Each of these factors was studied to comprehend their respective relationships concerning methanol electrooxidation.

Fig. 8a portrays cyclic voltammograms of the NiS-rGO-Ni/NF hybrid electrode immersed in a 1 M KOH solution, under the influence of varied methanol concentration. Evidently, the current density linked to methanol electrooxidation exhibits a distinct increase as the concentration of methanol rises up to 0.5 M, showing a maximum current density of about 220 mA cm^{-2}. Beyond this concentration, the current density becomes less responsive to further increases in methanol concentration, suggesting a saturation point has been reached (Fig. 8b). Another important observation from the voltammograms is the progressive reduction of the cathodic peak as methanol concentration increases. The process of methanol electrooxidation involves generating the electroactive Ni^{3+} species, which occurs by oxidizing Ni^{2+} originating form $Ni(OH)_2$ as well as Ni_3S_2/Ni_3S_4 (referred to as NiS) in the anodic region (potentials greater than 0.4 V), as depicted in reactions (14) and (15). These Ni^{3+} species then engage in a chemical reaction with methanol (reaction 16 and 17) [71], leading to the regeneration of Ni^{2+}. As result, there is an observable rise in the current density of the anodic peak, coupled with a decrease in the current density of the cathodic peak.

$$Ni(OH)_2 + OH^- \rightarrow NiOOH + H_2O + e^- \quad (14)$$

$$NiS + OH^- \rightarrow NiS(OH) + e^- \quad (15)$$

$$NiOOH + CH_3OH \rightarrow Ni(OH)_2 + Products \quad (16)$$

$$NiS(OH) + CH_3OH \rightarrow NiS + Products \quad (17)$$

In Fig. 8c, the impact of KOH concentration on methanol electrooxidation is evident. Initially, an increase in KOH concentration enhances the current density of methanol electrooxidation, reaching an optimal level before declining at higher KOH concentrations. This trend can be explained by the role of hydroxide ions (OH^-) in the reaction process.

Taking reaction (14) into consideration, and by assuming that the electrode material consists of pairs of coexisting solid solutions, the equilibrium potential of the material can be expressed in terms of the activity of the species (NiS and NiS(OH)) using the Nernst equation (18):

$$E = E^o + \frac{RT}{nF} \ln\left(\frac{a_{NiS(OH^-)}}{a_{NiS}\, a_{(OH^-)}}\right) \quad (18)$$

This equation elucidates that, from a thermodynamic perspective, an increase in the concentration of hydroxide ions (OH^-) would inherently induce a shift in the potential for methanol oxidation towards more negative values. Hence, as the concentration of OH^- ions is varied from

0.5 to 1.5 M, there was a shift in the potential of methanol electrooxidation accompanied with an elevation in the catalytic current density (Fig. 8d), indicating that the OH^- ions involve directly in the oxidation process [72]. The decrease in activity at higher concentrated solutions can be attributed to a higher concentration of hydroxide ions covering the surface. This leads to a reduction in the availability of active sites on the electrode for methanol adsorption, consequently affecting the process of methanol electrooxidation [73,74].

The catalyst loading significantly influences the electrooxidation of methanol, affecting overall electrocatalytic performance. To study this effect, we prepared a series of NiS-rGO-Ni/NF electrodes with varying NiS loadings by adjusting the number of cycles during potentiodynamic deposition. Specifically, we used 5, 10, 15, 20, 25, and 30 cycles of potential sweeping between 0 and -1 V. The obtained results (Fig. 9) showed a direct link between catalyst loading and methanol electrooxidation performance.

A noticeable increase in activity was observed as the number of cycles increased from 5 to 20. This emphasizes how controlled mass loading positively affect methanol oxidation reaction. The electrode prepared using 20 cycles demonstrated the highest level of electrocatalytic activity, representing the optimal performance point. However, beyond this point, there was a diminishing trend in activity, suggesting that there might be a limit where additional increase in catalyst loading could impede electrocatalytic activity. This observation could potentially be attributed to factors such as increased agglomeration of NiS particles and the subsequent drop-off of NiS particles as the cycle numbers increase.

Assessing an electrocatalyst's stability is a crucial aspect of evaluating its performance in the context of methanol oxidation reaction. We evaluated both the electrochemical and morphological stability of the NiS-rGO-Ni/NF electrode by subjecting it to prolonged electrolysis (chronoamperometry), in a solution containing 1 M KOH and 1 M methanol. This study was conducted under a constant potential of 0.6 V vs Ag/AgCl for a duration of 20 h.

The results, as depicted in Fig. 10a, reveal noteworthy characteristics of the NiS-rGO-Ni/NF catalyst. Over the 20 h measurement period, this catalyst consistently maintained a continuous and high current density. Remarkably, the current density displayed minimal decline throughout the entire duration. It's worth noting that the typical decrease in current density over time, which is commonly observed in such experiments, can be primarily attributed to the formation of hydrogen bubbles at the counter electrode. These bubbles tend to migrate and adhere to the working electrode's surface, ultimately diminishing the active surface area of the catalyst. In addition to electrochemical stability, we also investigated the morphological stability of the NiS-rGO-Ni/NF electrode to assess potential degradation or corrosion during the methanol oxidation reaction. SEM images were taken before and after the chronoamperometric test, as shown in Fig. S11. A comparison of these images indicates that the morphology of the NiS-rGO-Ni/NF electrode did not change after 20 h of methanol electrolysis, highlighting the remarkable morphological stability of this electrocatalysts. Surprisingly, the electrochemical behaviour of the electrode did not change at all after the 20 h of electrolysis (Fig. S12), further supporting the stable nature of the developed catalyst.

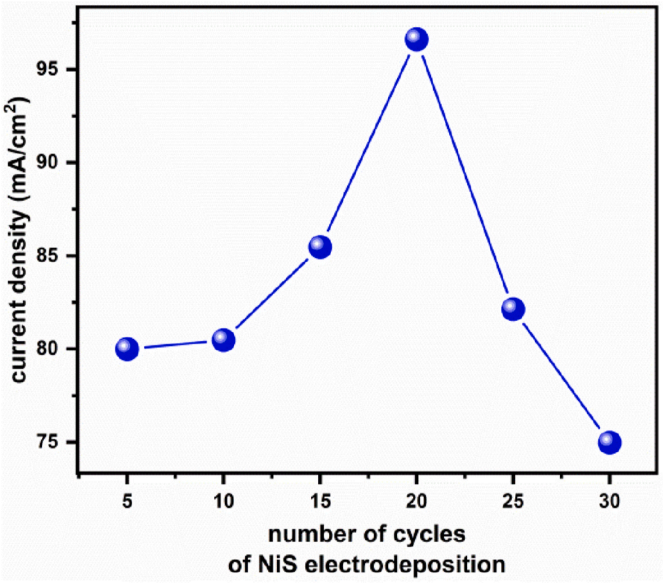

Fig. 9. Current density of methanol electrooxidation (1 M KOH + 0.1 M methanol at 0.6 V vs Ag/AgCl) using different cycles of NiS electrodeposition.

The stability of NiS-rGO-Ni/NF hybrid electrode was also examined by conducting 1000 cyclic voltammetry cycles within a fixed potential range of 0–0.8 V vs Ag/AgCl at a scan rate of 100 mV s^{-1}. The CV curves obtained at the 1st, 1000th, and 1001th cycles are depicted in Fig. 10b. After 1000 cycles, the current density decreased to approximately 83 %. This reduction in current could be partially attributed to the consumption of methanol and the formation of by-products during methanol oxidation. However, when the electrolyte was replaced with a fresh solution of 1 M KOH containing 0.5 M methanol, the electrode current density recovered to 92 %. The recovery of the current density to 92 % in the presence of a fresh solution of 1 M KOH with 0.5 M methanol indicates that the catalyst maintains its activity and stability under these conditions. This observation underscores the robustness of the catalyst.

A comparison of the catalytic performance between our developed NiS-rGO-Ni/NF catalyst and other nickel sulfide-based catalysts for the methanol oxidation reaction is presented in Table S1 of the supporting information. This table highlights how the NiS-rGO-Ni/NF catalyst stands out in terms of electrocatalytic activity when compared to previously reported nickel sulfide-containing materials.

3.2.7. *Computational study of the catalytic activity of methanol oxidation on Ni_3S_x surfaces*

The methanol oxidation reaction is a complex electrochemical process involving multiple intermediates and reaction pathways. To gain a deeper understanding of the catalytic behaviour of nickel sulfide (Ni_3S_x) surfaces, density functional theory (DFT) calculations were employed. This computational study focuses on elucidating the energetics and mechanisms of MOR on Ni_3S_2 (101) and Ni_3S_4 (001) surfaces. By analysing the Gibbs free energy diagrams for various intermediates, we aim to identify the most favourable reaction pathways and provide insights into the catalytic efficiency and durability of Ni_3S_x-based electrocatalysts.

In this study, the binding energy of CH_3OH molecules was calculated on Ni (111), Ni_3S_2 (101), Ni_3S_4 (001), and Pt(111) substrates. The binding energy (E_b) is determined using the equation:

$$E_b = E_{system} - E_{Substrate} - E_{CH3OH} \tag{19}$$

where E_{system} represents the energy of the substrate with the adsorbed CH_3OH molecules, $E_{subtrate}$ is the energy of the clean substrate, and E_{CH3OH} is the energy of the isolated CH_3OH molecule. A more negative E_{ads} indicates a stronger interaction between the molecule and the substrate.

The electrochemical oxidation process of CH_3OH involves several elementary steps, particularly on Ni_3S_2(101) and Ni_3S_4(001) substrates, as illustrated on Fig. 11. One of the key reactions is:

$$^*M - H + OH^-_{aq} \rightarrow {}^*M + H_2O_{aq} + e^- \tag{20}$$

Here, the change in reaction free energy (ΔG) can be expressed as:

$$\Delta G = G_{*M} + G_{H_2O} + G_{e^-} - G_{*M-H} - G_{OH^-} \tag{21}$$

Given that $G_{OH^-} = G_{H_2O} - G_{H_2}$, this can be simplified to:

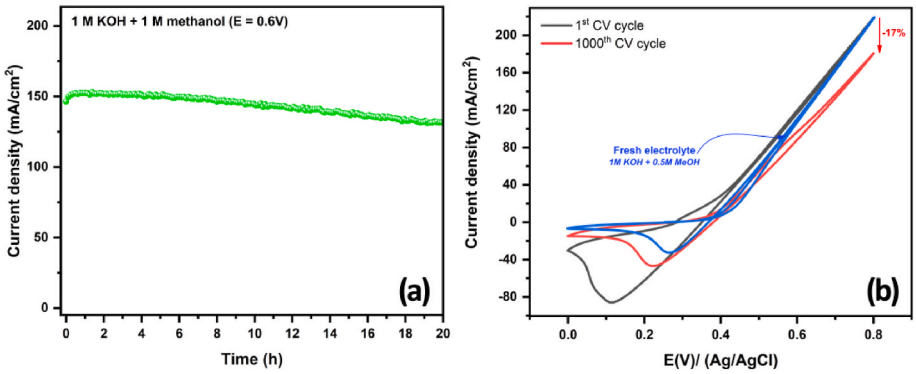

Fig. 10. (a) Long-term stability of NiS-rGO-Ni/NF hybrid electrode for 20 h. (b) Cyclic voltammetry profiles of NiS-rGO-Ni/NF hybrid electrode before and after 1000 cycles, conducted in the potential range of 0–0.8 V at a scan rate of 100 mV s^{-1} in a 1 M KOH solution containing 0.5 M methanol.

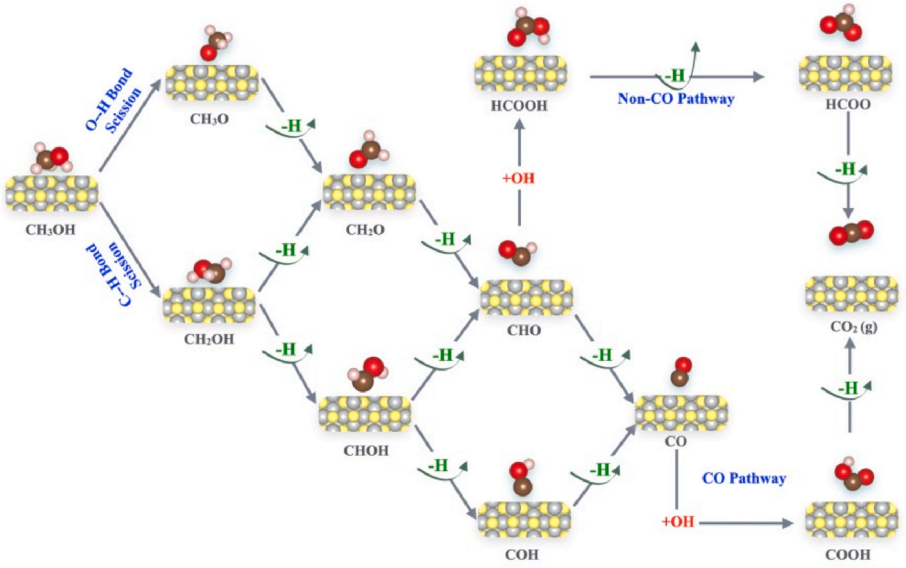

Fig. 11. Details mechanistic pathways of methanol oxidation on Ni_3S_x catalysts, highlighting both CO and non-CO pathways.

$$\Delta G = G_{*M} - G_{*M-H} + G_{H^+} + G_{e^-} \quad (22)$$

To compute the $G_{H^+} + G_{e^-}$ under standards conditions (pH = 0, U = 0), we used the computational hydrogen electrode (CHE) model developed by Nørskov [75]. According to this model, the chemical potential of $H^+ + e^-$ is given by:

$$G_{H^+} + G_{e^-} = \frac{1}{2} G_{H_2} \quad (23)$$

The reaction free energy correction (ΔG) is computed using the following formula:

$$\Delta G = \Delta E + \Delta ZPE + \Delta H\,(0 \rightarrow 298.15\,K) - T\Delta S \quad (24)$$

Where ΔE represent the adsorption energy, ΔZPE is the variation in zero-point energy, $\Delta H\,(0 \rightarrow 298.15\,K)$ denotes the integrated heat capacity from 0 to 298.15 K and ΔS is the change in entropy. A temperature (T) of 298.15 K is used in these calculations, these computed corrections are summarized in Table 2.

To elucidate the overall methanol oxidation reaction (MOR) mechanism, we employed first-principles calculation integrated with the computational hydrogen electrode model, two distinct nickel sulfide models, Ni_3S_2 (101) and Ni_3S_4 (001), were constructed to simulate catalytic activity, with pure Ni (111) and Pt (111) surfaces included for comparison. The initial step in the methanol oxidation reaction involves the adsorption of methanol on the catalyst surface. Our computation of methanol adsorption on these surfaces revealed that the CH_3OH molecule consistently adsorbs atop the Ni atom through oxygen bonding. Six different configurations of CH_3OH adsorbed on Ni_3S_2 (101) and Ni_3S_4

Table 2
Computed thermodynamic corrections, Zero-Point Energy (*ZPE*), Heat-capacity (C_p), and entropy (S) at 298 K Free Molecules and Adsorbed intermediates (eV).

Elements	*ZPE*	$\int C_p dT(0 \rightarrow 298.15\,K)$	*TS*
CO_2	0.314	0.102	0.620
H_2O	0.572	0.118	0.639
H_2	0.272	0.091	0.433
CO	0.135	0.087	0.682
CH_3OH	1.361	0.119	0.750
HCOOH	0.920	0.127	1.009
*CH_3OH	1.381	0.120	0.315
*CH_2OH	1.114	0.108	0.229
*CH_3O	1.103	0.113	0.210
*CH_2O	0.706	0.088	0.248
*CO_2	0.311	0.059	0.102
*CHOH	0.786	0.092	0.165
*CHO	0.471	0.063	0.171
*CO	0.191	0.080	0.138
*HCOO	0.594	0.109	0.226
*HCOOH	0.910	0.101	0.209
*COOH	0.607	0.099	0.209
*COH	0.482	0.090	0.122

(001) surfaces, with different orientations and active sites with regards to their relative energies, are depicted in Fig. 12(a–g) and 13(a-g). These configurations ensure a stable interaction that is essential for the subsequent steps of the oxidation process. Our findings demonstrate that both Ni_3S_2 (101) and Ni_3S_4 (001) surfaces exhibits significantly more negative adsorption energies of −0.537 eV and −1.147 eV, respectively, compared to −0.223 eV for Ni (111) and −0.375 eV for Pt (111).

This substantial increase in adsorption energy with higher sulfur content indicates a stronger interaction between methanol and the Ni–S surfaces, enhancing the catalytic performance of nickel sulfide over pure nickel and platinum. Additionally, we analysed the charge distribution of neighbouring Ni–S atoms after CH_3OH adsorption on both Ni_3S_2 (101) and Ni_3S_4 (001) surfaces by examining the distributed charge density, as shown in Figs. 12h and 13h. Our findings indicate that the Ni-atoms surrounding the adsorbed CH_3OH molecule contribute partial electron densities to the CH_3OH.

Another crucial mechanistic step is the transfer of a proton and electron to the adsorbed CO intermediates [76,77]. Furthermore, we computed CO adsorption energies on these surfaces to further understand the catalytic properties. Ni_3S_2 (101) and Ni_3S_4 (001) exhibited more negative adsorption energies than Ni (111) and Pt (111), suggesting a higher reactivity and potential for CO tolerance, which is critical for MOR efficiency. These findings, summarized in Table 3, highlight the superior catalytic properties of nickel sulfide surfaces for methanol oxidation, attributed to their higher adsorption energy for methanol. These insights provide a deeper understanding of the role of sulfur in enhancing the catalytic activity of nickel-based surfaces, offering potential pathways for the design of more efficient MOR catalysts. Fig. 13

Understanding the intricate mechanisms behind methanol electrooxidation (MOR) is crucial for developing efficient and selective electrocatalysts. In this regard, Gibbs free energy diagrams reveal a thermodynamically favourable overall conversion of CH_3OH to CO_2,

Table 3
Details comparison of binding energies (E_b) and corresponding oxygen/carbon-metal distances ($d_{Ni/Pt-O/C}$) for methanol (CH_3OH) and carbon monoxide (CO) molecules adsorbed on Ni (111), Ni_3S_2 (101), Ni_3S_4 (001), and Pt (111) substrates. The data provide insights into these different surface's interaction strengths and adsorption configurations.

CH_3OH	Ni (111)	Ni_3S_2 (101)	Ni_3S_4 (001)	Pt (111)
$E_b(eV)$	−0.223	−0.537	−1.147	−0.375
$d_{Ni/Pt-O}(Å)$	2.147	2.043	2.101	2.383
CO				
$E_b(eV)$	−1.348	−1.575	−1.786	−1.462
$d_{Ni/Pt-C}(Å)$	1.734	1.763	1.787	1.822

indicating the spontaneous nature of MOR via several reactions pathways. We meticulously explored the potential elementary steps for MOR on both Ni_3S_2 (101) and Ni_3S_4 (001) surfaces, considering both deprotonation and hydroxyl addition pathways. Notably, both surfaces, an alternative non-CO pathway was identified:

$$CH_3OH(g) \rightarrow *CH_3OH \rightarrow *CH_2OH \rightarrow *CH_2O \rightarrow *CHO \rightarrow *HCOOH \rightarrow *HCOO \rightarrow CO_2(g)$$

Here, "*" denotes adsorbed species on the catalyst surface. The analysis of the Gibbs free energy diagrams (Fig. 14) reveals a key finding: the overall conversion of CH_3OH to CO_2 is thermodynamically favourable for both Ni_3S_2 (101) and Ni_3S_4 (001) surfaces. This translates to a spontaneous process, where the reaction proceeds downhill in terms of free energy. Interestingly, the diagrams unveil not just a single pathway, but rather a network of potential reaction coordinates for MOR. We meticulously investigated both deprotonation and hydroxyl addition pathways, encompassing a comprehensive exploration of the possible reaction mechanisms.

A significant outcome of this investigation is the identification of an

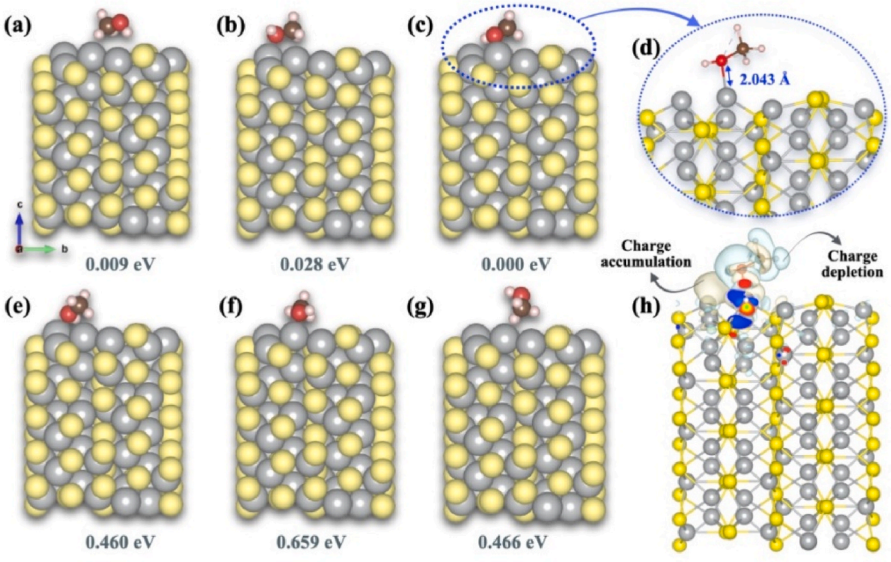

Fig. 12. (a–g) Optimized structure of six different CH_3OH configurations adsorbed on the Ni_3S_2 (101) surface, illustrating various orientations and active sites with their respective relative energies. (h) Charge density distribution of CH_3OH and the Ni_3S_2 (101) surface, where yellow and cyan contours represent reduced and enhanced charge densities, respectively, at an iso-surface value of 0.007 e.$Å^{-3}$. The H, O, C, Ni, and S atoms are shown in white, red, brown, grey, and yellow, respectively. (For interpretation of the references to colour in this figure legend, the reader is referred to the Web version of this article.)

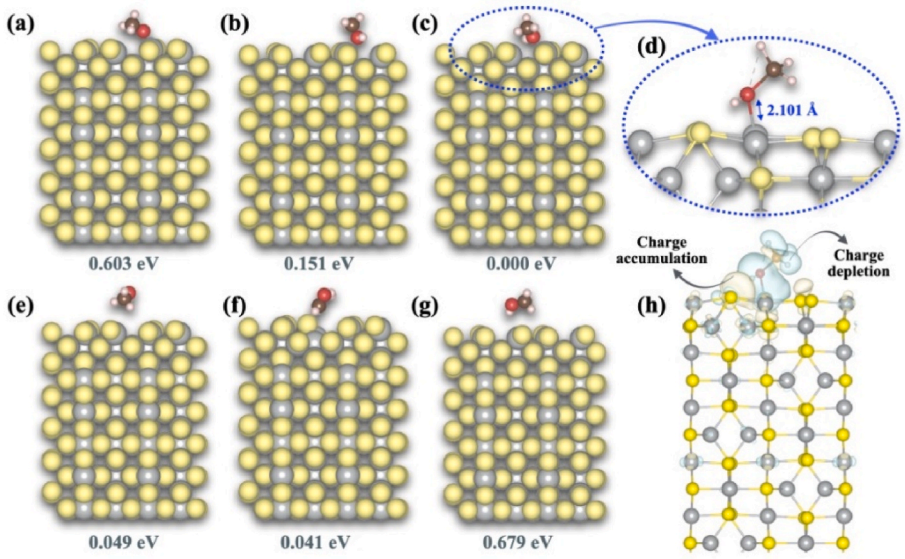

Fig. 13. (a–g) Optimized structure of six different CH_3OH configurations adsorbed on the Ni_3S_4 (001) surface, illustrating various orientations and active sites with their respective relative energies. (h) Charge density distribution of CH_3OH and the Ni_3S_4 (001) surface, where yellow and cyan contours represent reduced and enhanced charge densities, respectively, at an iso-surface value of 0.007 e.Å^{-3}. The H, O, C, Ni, and S atoms are shown in white, red, brown, grey, and yellow, respectively. (For interpretation of the references to colour in this figure legend, the reader is referred to the Web version of this article.)

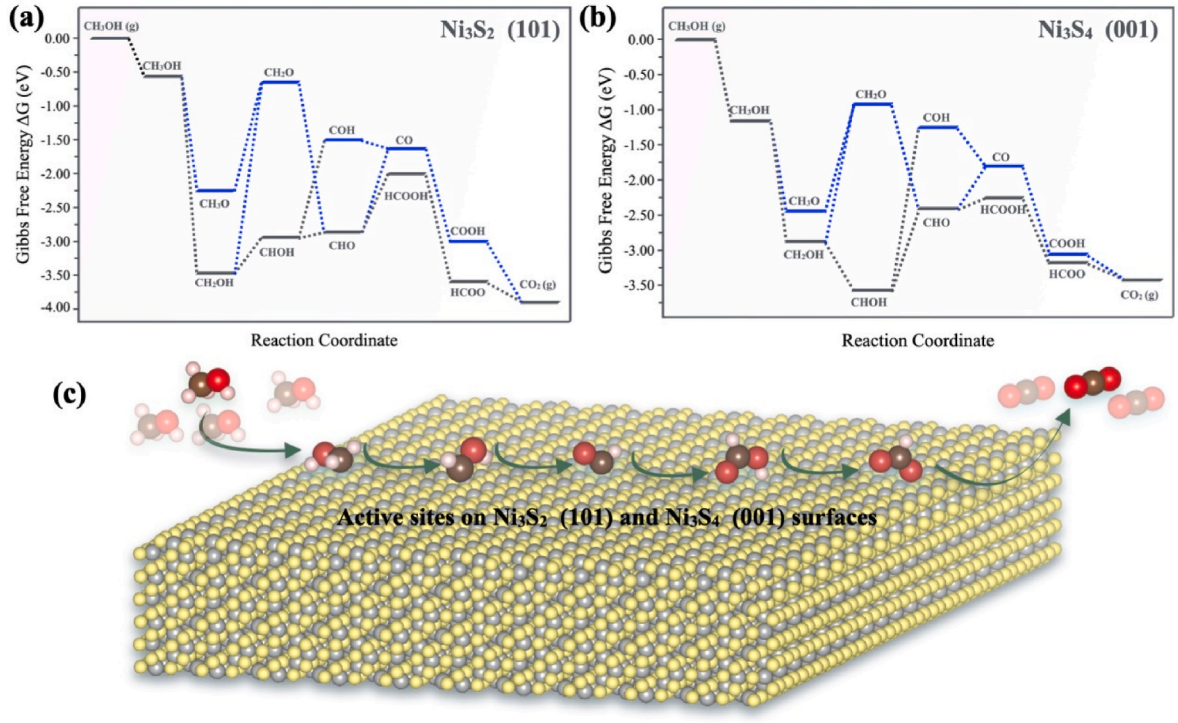

Fig. 14. (a, b) Gibbs Free-energy diagrams of all possible pathways for the Methanol Oxidation Reaction (MOR) by sequential poton and electron transfer at 0.0 V versus RHE for the Ni_3S_2 (101) and Ni_3S_4 (001) surface catalysts. (c) A schematic diagram showing the tentative reaction mechanism for methanol oxidation on nickel sulfide surface catalysts.

alternative non-CO pathway for MOR on both Ni_3S_2 (101) and Ni_3S_4 (001) surfaces. This pathway deviates from the traditional route involving CO as an intermediate, potentially mitigating the detrimental effects of CO poisoning which can hinder MOR activity. As depicted in Fig. 14, the non-CO pathway proceeds through a series of elementary steps involving adsorbed intermediates like $*CH_2OH$, $*CH_2O$, *CHO, *HCOOH, and *HCOO. Notably, the free energy changes for each step in this pathway exhibit a remarkable characteristic – they are relatively similar.

This observation suggests a series of facile elementary reactions, signifying a smooth and efficient progression of MOR on both studied surfaces. Furthermore, a close examination of Fig. 14, might reveal specific intermediates with particularly high or low free energy values. For instance, a particularly stable $*CH_2OH$ intermediates could indicates a rate-determining step associated with its conversion. Identifying such bottlenecks in the reaction sequence paves the way for targeted catalyst

design strategies to overcome these limitations and enhance overall MOR efficiency.

In conclusion, the exploration of Gibbs free energy diagrams provided a comprehensive understanding of the MOR mechanism on Ni_3S_2 (101) and Ni_3S_4 (001) surfaces. The presence of multiple reaction pathways, particularly the facile non-CO pathway, highlights the versatility of these materials for MOR catalysis. Identifying particularly stable intermediates and the rate-determining step from the diagrams paves the way for further research aimed at engineering more efficient and selective electrocatalysts for fuel cell applications.

4. Conclusion

This study delves into the development and electrochemical assessment of a novel NiS-rGO-Ni/NF hybrid electrode material aimed at improving methanol electrooxidation. The hybrid material was deliberately constructed to maximize surface area and improve electron transfer efficiency. This involved utilizing DHBT deposition to create a porous structure, followed by the addition of graphene oxide to further enhance electron transfer with the electrode material. XRD analysis revealed that the nickel sulfide phase formed after electrodeposition consisted of a combination of Ni_3S_2 and Ni_3S_4 phases. SEM images of NiS-rGO-Ni/NF revealed a distinct highly porous dendritic structure, contributing to its notable high surface area. XPS analysis definitively validated the effective integration of reduced graphene into the electrodeposited material, solidifying its presence within the composite structure. Through a thorough examination analysis using cyclic voltammetry, the NiS-rGO-Ni/NF electrode showed enhanced electrochemical performance compared to NiS/NF. The integration of rGO and the porous nickel layer into the NiS/NF structure significantly enhanced the hybrid electrode's capabilities. Specifically, it lowered the onset potential of Ni^{3+} formation, which is crucial for methanol oxidation. Additionally, it increased the surface concentration of Ni^{3+} on the electrode's surface by a factor of 20, while substantially improving the electrochemical surface area from 22 cm^2 (NiS/NF) to 179 cm^2 (NiS-GO-Ni/NF). Electrochemical impedance spectroscopy further validated the electrode's efficient electron transfer during Ni^{2+} to Ni^{3+} conversion, as evidenced by its low charge transfer resistance. Specifically, the NiS-rGO-Ni/NF electrode exhibited a charge transfer resistance of 25.47 Ω cm^2, whereas the NiS/NF electrode displayed a much higher resistance of 4830 Ω cm^2. Methanol electrooxidation experiments underscored the catalyst's superior performance, achieving higher current densities and lower Tafel slope (220 mA cm^{-2}, 122 mV.dec^{-1}) compared to the NiS/NF electrode (114 mA cm^{-2}, 204 mV.dec^{-1}). The combination of reduced graphene oxide and porous nickel proved advantageous in dispersing the active component, leading to improved electrocatalytic performances. Density functional theory (DFT) calculations were employed to investigate the catalytic activity of methanol oxidation on Ni_3S_x surfaces. The Gibbs free energy diagrams indicated multiple spontaneous pathways for the conversion of CH_3OH to CO_2, highlighting the role of Ni_3S_x surfaces in facilitating MOR. The theoretical insights provided a deeper understanding of the reaction mechanisms, supporting the experimental findings. The study evaluated the stability of the NiS-rGO-Ni/NF hybrid electrode over 20 h of electrolysis, demonstrating its robustness. Overall, the electrode shows promise for efficient methanol electrooxidation and provides valuable insights for enhancing electrochemical performance through catalyst design and optimization.

CRediT authorship contribution statement

Mehdi Salmi: Writing – original draft, Validation, Investigation, Formal analysis. **Nabil Khossossi:** Writing – original draft, Validation, Investigation. **Yousra Boudad:** Writing – review & editing, Investigation. **Charafeddine Jama:** Writing – review & editing, Investigation. **Fouad Bentiss:** Writing – original draft, Validation, Investigation. **Zaina Zaroual:** Writing – review & editing, Validation, Investigation. **Sanae El Ghachtouli:** Writing – review & editing, Writing – original draft, Supervision, Methodology, Conceptualization.

Data availability

Data will be made available on request.

Declaration of AI use

We have not used AI-assisted technologies in creating this article.

Declaration of competing interest

The authors declare that they have no known competing financial interests or personal relationships that could have appeared to influence the work reported in this paper.

Acknowledgements

The authors gratefully acknowledge the National Center for Scientific and Technical Research (*CNRST*) of Morocco for providing access to the technical facilities of the *UATRS* division. Additionally, the authors extend their sincere thanks to N. Khossossi for conducting the essential theoretical calculations for the *DFT* section. The authors also wish to express their gratitude to Pr. C. Jama and Pr. F. Bentiss for their invaluable assistance with *XPS* measurements.

Appendix A. Supplementary data

Supplementary data to this article can be found online at https://doi.org/10.1016/j.ijhydene.2024.12.285.

References

[1] Höök M, Tang X. Depletion of fossil fuels and anthropogenic climate change—a review. Energy Pol 2013;52:797–809. https://api.semanticscholar.org/CorpusID:154464711.
[2] Vohra K, Vodonos A, Schwartz J, Marais EA, Sulprizio MP, Mickley LJ. Global mortality from outdoor fine particle pollution generated by fossil fuel combustion: results from GEOS-Chem. Environ Res 2021:110754. https://api.semanticscholar.org/CorpusID:231909881.
[3] Holechek JL, Geli HME, Sawalhah MN, Valdez R. A global assessment: can renewable energy replace fossil fuels by 2050? Sustainability 2022;14. https://doi.org/10.3390/su14084792.
[4] Fan L, Tu Z, Chan SH. Recent development of hydrogen and fuel cell technologies: a review. Energy Rep 2021;7:8421–46.
[5] Shaari N, Kamarudin SK, Bahru R, Osman SH, Md Ishak NAI. Progress and challenges: review for direct liquid fuel cell. Int J Energy Res 2021;45:6644–88.
[6] Alias MS, Kamarudin SK, Zainoodin AM, Masdar MS. Active direct methanol fuel cell: an overview. Int J Hydrogen Energy 2020;45:19620–41.
[7] Smith WA, Burdyny T, Vermaas DA, Geerlings H. Pathways to industrial-scale fuel out of thin air from CO2 electrolysis. Joule 2019;3:1822–34.
[8] Shi J, Zhu Y, Feng Y, Yang J, Xia C. A prompt decarbonization pathway for shipping: green hydrogen, ammonia, and methanol production and utilization in marine engines. Atmosphere 2023;14. https://doi.org/10.3390/atmos14030584.
[9] Kamarudin SK, Achmad F, Daud WRW. Overview on the application of direct methanol fuel cell (DMFC) for portable electronic devices. Int J Hydrogen Energy 2009;34:6902–16.
[10] Bagkar NC, Chen HM, Parab H, Liu R-S. Nanostructured electrocatalyst synthesis: fundamental and methods. In: Electrocatal. Direct methanol fuel cells. John Wiley & Sons, Ltd; 2009. p. 79–114.
[11] Kamarudin SK, Daud WRW, Ho SL, Hasran UA. Overview on the challenges and developments of micro-direct methanol fuel cells (DMFC). J Power Sources 2007;163:743–54.
[12] Xia Z, Zhang X, Sun H, Wang S, Sun G. Recent advances in multi-scale design and construction of materials for direct methanol fuel cells. Nano Energy 2019;65:104048.
[13] Housmans THM, Koper MTM. Methanol oxidation on stepped Pt[n(111) × (110)] electrodes: a chronoamperometric study. J Phys Chem B 2003;107:8557–67. https://doi.org/10.1021/jp034291k.
[14] Yaqoob L, Noor T, Iqbal N. Recent progress in development of efficient electrocatalyst for methanol oxidation reaction in direct methanol fuel cell. Int J Energy Res 2021;45:6550–83.
[15] Salarvand V, Abedini Mohammadi M, Yousefifar A, Yazdi MS, Mostafaei A. Facile hydrothermal synthesis of combined MoSe2PS nanostructures on nickel foam with

superior electrocatalytic properties for hydrogen evolution reaction. Int J Hydrogen Energy 2023;48:10038–50.
[16] Salarvand V, Abedini Mohammadi M, Ahmadian F, Rajabi Kouchi F, Saghafi Yazdi M, Mostafaei A. In-situ hydrothermal synthesis of NiCo(X)Se compound on nickel foam for efficient performance of water splitting reaction in alkaline media. J Electroanal Chem 2022;926:116929.
[17] Abedini Mohammadi M, Saghafi Yazdi M, Talafi Noghani M, Moghanian A, Hosseini SA. Synthesis and optimization of Mo–Ni–Se@NiSe core-shell nanostructures as efficient and durable electrocatalyst for hydrogen evolution reaction in alkaline media. Int J Hydrogen Energy 2022;47:34455–70.
[18] Cheng Y, Zhai M, Hu J. The fabrication of NiCu 2 S 2 from NiCu film on nickel foam for methanol electrooxidation and supercapacitors. Appl Surf Sci 2019;480: 505–13. https://doi.org/10.1016/j.apsusc.2019.03.022.
[19] Jin D, Li Z, Wang Z. Hierarchical NiCo2O4 and NiCo2S4 nanomaterials as electrocatalysts for methanol oxidation reaction. Int J Hydrogen Energy 2021;46: 32069–80.
[20] Du J, You S, Li X, Tang B, Jiang B, Yu Y, Cai Z, Ren N, Zou J. In situ crystallization of active NiOOH/CoOOH heterostructures with hydroxide ion adsorption sites on velutipes-like CoSe/NiSe nanorods as catalysts for oxygen evolution and cocatalysts for methanol oxidation. ACS Appl Mater Interfaces 2020;12:686–97. https://doi.org/10.1021/acsami.9b16626.
[21] Azizi S, Askari MB, Moghadam MTT, Seifi M, Di Bartolomeo A. Ni3S4/NiS/rGO as a promising electrocatalyst for methanol and ethanol electro-oxidation. Nano Futur 2023;7:15002. https://doi.org/10.1088/2399-1984/acb02b.
[22] Zhang J, Xu C, Zhang D, Zhao J, Zheng S, Su H, Wei F, Yuan B, Fernandez C. Facile synthesis of a nickel sulfide (NiS) hierarchical flower for the electrochemical oxidation of H 2 O 2 and the methanol oxidation reaction (MOR). J Electrochem Soc 2017;164:B92–6. https://doi.org/10.1149/2.0221704jes.
[23] AlMalki MA, Khan ZA, El-Said WA. Synthesis and characterization of Nickel sulfide and Nickel sulfide/Molybdenum disulfide nanocomposite modified ITO electrode as efficient anode for methanol electrooxidation. Appl. Surf. Sci. Adv. 2021;6: 100187.
[24] Tiwari JN, Tiwari RN, Kim KS. Zero-dimensional, one-dimensional, two-dimensional and three-dimensional nanostructured materials for advanced electrochemical energy devices. Prog Mater Sci 2012;57:724–803.
[25] Xie C, Niu Z, Kim D, Li M, Yang P. Surface and interface control in nanoparticle catalysis. Chem Rev 2020;120:1184–249. https://doi.org/10.1021/acs.chemrev.9b00220.
[26] Askari MB, Rozati SM. Construction of Co3O4-Ni3S4-rGO ternary hybrid as an efficient nanoelectrocatalyst for methanol and ethanol oxidation in alkaline media. J Alloys Compd 2022;900:163408.
[27] Mao H, Cao Z, Guo X, Liu M, Sun D, Sun Z, Ge H, Zhang Y, Song XM. Enhanced electrocatalytic performance for the oxidation of methanol by hierarchical NiS/Ni (OH) 2 @polypyrrole/graphene oxide nanosheets. Appl Surf Sci 2019;471:355–67. https://doi.org/10.1016/j.apsusc.2018.11.188.
[28] Salmi M, Amarray A, Samih Y, Azzi M, EL Ghachtouli S. Electrodeposited nickel sulfide nanoparticles incorporated carbon nanofibers as effective non-precious catalyst for methanol electrooxidation in alkaline medium. ChemistrySelect 2023; 8:e202204769.
[29] Plowman BJ, Jones LA, Bhargava SK. Building with bubbles: the formation of high surface area honeycomb-like films via hydrogen bubble templated electrodeposition. Chem Commun 2015;51:4331–46. https://doi.org/10.1039/C4CC06638C.
[30] Varzi A, Mattarozzi L, Cattarin S, Guerriero P, Passerini S. 3D porous Cu–Zn alloys as alternative anode materials for Li-ion batteries with superior low T performance. Adv Energy Mater 2018;8:1701706.
[31] Moreno-García P, Schlegel N, Zanetti A, Cedeno López A, Gálvez-Vázquez MDJ, Dutta A, Rahaman M, Broekmann P. Selective electrochemical reduction of CO2 to CO on Zn-based foams produced by Cu2+ and template-assisted electrodeposition. ACS Appl Mater Interfaces 2018;10:31355–65. https://doi.org/10.1021/acsami.8b09894.
[32] Siwek KI, Eugénio S, Santos DMF, Silva MT, Montemor MF. 3D nickel foams with controlled morphologies for hydrogen evolution reaction in highly alkaline media. Int J Hydrogen Energy 2019;44:1701–9.
[33] Arévalo-Cid P, Vaz MF, Montemor MF. Highly porous FeNi 3D foams produced by one-step electrodeposition: electrochemical stability and mechanical properties. Mater Char 2022;193:112311.
[34] Wu H, Li Y, Chen L, Diao Q, Zhuang B. In situ fabrication of transition metal phosphide tree-like nanostructure for energy-saving hydrogen production coupled via urea oxidation reaction. J Electroanal Chem 2024;963:118286.
[35] Ait Himi M, El Ghachtouli S, Amarray A, Zaroual Z, Bonnaillie P, Azzi M. Removal of azo dye calcon using polyaniline films electrodeposited on SnO2 substrate. Phys. Chem. Res. 2020;8:111–24. https://doi.org/10.22036/pcr.2019.203023.1680.
[36] Hummers WSJ, Offeman RE. Preparation of graphitic oxide. J Am Chem Soc 1958; 80:1339. https://doi.org/10.1021/ja01539a017.
[37] Zhang Y, Ji Y, Wang Z, Liu S, Zhang T. Electrodeposition synthesis of reduced graphene oxide–carbon nanotube hybrids on indium tin oxide electrode for simultaneous electrochemical detection of ascorbic acid{,} dopamine and uric acid. RSC Adv 2015;5:106307–14. https://doi.org/10.1039/C5RA24727F.
[38] Tourabi M, Nohair K, Traisnel M, Jama C, Bentiss F. Electrochemical and XPS studies of the corrosion inhibition of carbon steel in hydrochloric acid pickling solutions by 3,5-bis(2-thienylmethyl)-4-amino-1,2,4-triazole. Corrosion Sci 2013; 75:123–33.
[39] Kresse G, Hafner J. Ab initio molecular dynamics for open-shell transition metals. Phys Rev B Condens Matter 1993;48 17:13115–8. https://api.semanticscholar.org/CorpusID:22093607.
[40] Kresse G, Furthmüller J. Efficiency of ab-initio total energy calculations for metals and semiconductors using a plane-wave basis set. Comput Mater Sci 1996;6:15–50.
[41] Kresse G, Furthmüller J. Efficient iterative schemes for ab initio total-energy calculations using a plane-wave basis set. Phys Rev B Condens Matter 1996;54: 11169–86. https://doi.org/10.1103/physrevb.54.11169.
[42] Blöchl PE. Projector augmented-wave method. Phys Rev B 1994;50:17953–79. https://doi.org/10.1103/PhysRevB.50.17953.
[43] Perdew JP, Burke K, Ernzerhof M. Generalized gradient approximation made simple. Phys Rev Lett 1996;77:3865–8. https://doi.org/10.1103/PhysRevLett.77.3865.
[44] Wang V, Xu N, Liu J-C, Tang G, Geng W-T. VASPKIT: a user-friendly interface facilitating high-throughput computing and analysis using VASP code. Comput Phys Commun 2021;267:108033.
[45] Stankovich S, Dikin DA, Piner RD, Kohlhaas KA, Kleinhammes A, Jia Y, Wu Y, Nguyen ST, Ruoff RS. Synthesis of graphene-based nanosheets via chemical reduction of exfoliated graphite oxide. Carbon N. Y. 2007;45:1558–65.
[46] Chen L, Tang Y, Wang K, Liu C, Luo S. Direct electrodeposition of reduced graphene oxide on glassy carbon electrode and its electrochemical application. Electrochem Commun 2011;13:133–7.
[47] Toh SY, Loh KS, Kamarudin SK, Daud WRW. Graphene production via electrochemical reduction of graphene oxide: synthesis and characterisation. Chem Eng J 2014;251:422–34.
[48] Mirzaee M, Dehghanian C, Sabet Bokati K. One-step electrodeposition of reduced graphene oxide on three-dimensional porous nano nickel-copper foam electrode and its use in supercapacitor. J Electroanal Chem 2018;813:152–62.
[49] Sultana UK, He T, Du A, O'Mullane AP. An amorphous dual action electrocatalyst based on oxygen doped cobalt sulfide for the hydrogen and oxygen evolution reactions. RSC Adv 2017;7:54995–5004. https://doi.org/10.1039/C7RA10394H.
[50] García-Valenzuela JA. Simple thiourea hydrolysis or intermediate complex mechanism? Taking up the formation of metal sulfides from metal–thiourea alkaline solutions. Comments Mod Chem 2017;37:99–115. https://doi.org/10.1080/02603594.2016.1230547.
[51] Nourshargh B, Ghaffarinejad A, Barati Darband G. Water splitting by CoFeLDH@NiFeS nanoelectrocatalyst assisted urea electrooxidation reaction. J Environ Chem Eng 2024;12:111629.
[52] Edison TNJI, Atchudan R, Karthik N, Ganesh K, Xiong D, Lee YR. A novel binder-free electro-synthesis of hierarchical nickel sulfide nanostructures on nickel foam as a battery-type electrode for hybrid-capacitors. Fuel 2020;276:118077. https://doi.org/10.1016/j.fuel.2020.118077.
[53] Park GD, Cho JS, Kang YC. Sodium-ion storage properties of nickel sulfide hollow nanospheres/reduced graphene oxide composite powders prepared by a spray drying process and the nanoscale Kirkendall effect. Nanoscale 2015;7:16781–8. https://doi.org/10.1039/C5NR04252F.
[54] Venkata-Haritha M, Gopi CVVM, Kim S-K, Lee J, Kim H-J. Solution-processed morphology-controllable nanosphere structured highly efficient and stable nickel sulfide counter electrodes for dye- and quantum dot-sensitized solar cells. New J Chem 2015;39:9575–85. https://doi.org/10.1039/C5NJ01961C.
[55] Ganesan P, Sivanantham A, Shanmugam S. Inexpensive electrochemical synthesis of nickel iron sulphides on nickel foam: super active and ultra-durable electrocatalysts for alkaline electrolyte membrane water electrolysis. J Mater Chem A 2016;4:16394–402. https://doi.org/10.1039/c6ta04499a.
[56] Xiong D, Li W, Liu L. Vertically aligned porous nickel(II) hydroxide nanosheets supported on carbon paper with long-term oxygen evolution performance. Chem Asian J 2017;12:543–51.
[57] Fingerle M, Tengeler S, Calvet W, Mayer T, Jaegermann W. Water interaction with sputter-deposited nickel oxide on n-Si photoanode: cryo photoelectron spectroscopy on adsorbed water in the frozen electrolyte approach. J Electrochem Soc 2018;165:H3148. https://doi.org/10.1149/2.0191804jes.
[58] Kim D, Karthick Kannan P, Mateti S, Chung C-H. Indirect nanoconstruction morphology of Ni3S2 electrodes renovates the performance for electrochemical energy storage. ACS Appl Energy Mater 2018;1:6945–52. https://doi.org/10.1021/acsaem.8b01310.
[59] Ahmed N, Ali BA, Ramadan M, Allam NK. Three-dimensional interconnected binder-free Mn-Ni-S nanosheets for high performance asymmetric supercapacitor devices with exceptional cyclic stability. ACS Appl Energy Mater 2019;2:3717–25. https://doi.org/10.1021/acsaem.9b00435.
[60] Hou G-Y, Lyu Z-Y, Tang Y-P, Cao H-Z, Zheng G-Q. Preparation of flexible composite electrode with bacterial cellulose (BC)-derived carbon aerogel supported low loaded NiS for methanol electrocatalytic oxidation. Int J Hydrogen Energy 2020; 45:16049–59.
[61] Yavuz A, Ozdemir N, Erdogan PY, Zengin H, Zengin G, Bedir M. Nickel-based materials electrodeposited from a deep eutectic solvent on steel for energy storage devices. Appl Phys A 2019;125:494. https://doi.org/10.1007/s00339-019-2787-2.
[62] Lee M, Oh HS, Cho MK, Ahn JP, Hwang YJ, Min BK. Activation of a Ni electrocatalyst through spontaneous transformation of nickel sulfide to nickel hydroxide in an oxygen evolution reaction. Appl Catal B Environ 2018;233:130–5. https://doi.org/10.1016/j.apcatb.2018.03.083.
[63] Yan B, Krishnamurthy D, Hendon CH, Deshpande S, Surendranath Y, Viswanathan V. Surface restructuring of nickel sulfide generates optimally coordinated active sites for oxygen reduction catalysis. Joule 2017;1:600–12.
[64] Anantharaj S, Sugime H, Noda S. Surface amorphized nickel hydroxy sulphide for efficient hydrogen evolution reaction in alkaline medium. Chem Eng J 2021;408: 127275.
[65] Trafela Š, Zavašnik J, Šturm S, Rožman KŽ. Formation of a Ni(OH)2/NiOOH active redox couple on nickel nanowires for formaldehyde detection in alkaline media. Electrochim Acta 2019;309:346–53.

[66] Bard AJ, Faulkner LR. Electrochemical methods: fundamentals and applications. Wiley; 2000. https://books.google.co.ma/books?id=kv56QgAACAAJ.
[67] Ko JS, Doan-Nguyen VVT, Kim H-S, Petrissans X, DeBlock RH, Choi CS, Long JW, Dunn BS. High-rate capability of Na2FePO4F nanoparticles by enhancing surface carbon functionality for Na-ion batteries. J Mater Chem A 2017;5:18707–15. https://doi.org/10.1039/C7TA05680J.
[68] Akbar F, Tariq M, khan HU, Khan J, Uddin MK, Ahmed SS, Rahim A. Development of Ag–Ni NPs loaded on MWCNTs for highly sensitive, selective and reproducible non-enzymatic electrochemical detection of glucose. J Mater Sci Mater Electron 2021;32:16166–81. https://doi.org/10.1007/s10854-021-06164-2.
[69] Cui X, Xiao P, Wang J, Zhou M, Guo W, Yang Y, He Y, Wang Z, Yang Y, Zhang Y, Lin Z. Highly branched metal alloy networks with superior activities for the methanol oxidation reaction. Angew Chem Int Ed 2017;56:4488–93.
[70] Li J, Zuo Y, Liu J, Wang X, Yu X, Du R, Zhang T, Infante-Carrió MF, Tang P, Arbiol J, Llorca J, Luo Z, Cabot A. Superior methanol electrooxidation performance of (110)-faceted nickel polyhedral nanocrystals. J Mater Chem A 2019;7:22036–43. https://doi.org/10.1039/c9ta07066d.
[71] Boggs BK, King RL, Botte GG. Urea electrolysis: direct hydrogen production from urine. Chem Commun 2009:4859–61. https://doi.org/10.1039/B905974A.
[72] Wu F, Zhang Z, Zhang F, Duan D, Li Y, Wei G, Liu S, Yuan Q, Wang E, Hao X. New insights into the electrocatalytic mechanism of methanol oxidation on amorphous Ni-B-Co nanoparticles in alkaline media. Catalysts 2019;9. https://doi.org/10.3390/catal9090749.
[73] Sunitha M, Sathish A, Ramachandran T. Nickel boride and cobalt boride coated stainless steel gauze for enhanced electrochemical oxidation of methanol. Ionics 2020;26:1875–84. https://doi.org/10.1007/s11581-019-03410-w.
[74] Rus ED, Wakabayashi RH, Wang H, Abruña HD. Methanol oxidation at platinum in alkaline media: a study of the effects of hydroxide concentration and of mass transport. ChemPhysChem 2021. https://doi.org/10.1002/cphc.202100087.
[75] Nørskov JK, Rossmeisl J, Logadottir A, Lindqvist L, Kitchin JR, Bligaard T, Jónsson H. Origin of the overpotential for oxygen reduction at a fuel-cell cathode. J Phys Chem B 2004;108:17886–92. https://doi.org/10.1021/jp047349j.
[76] Koper MTM, Shubina TE, van Santen RA. Periodic density functional study of CO and OH adsorption on Pt−Ru alloy surfaces: implications for CO tolerant fuel cell catalysts. J Phys Chem B 2002;106:686–92. https://doi.org/10.1021/jp0134188.
[77] Xie J, Zhang Q, Gu L, Xu S, Wang P, Liu J, Ding Y, Yao YF, Nan C, Zhao M, You Y, Zou Z. Ruthenium–platinum core–shell nanocatalysts with substantially enhanced activity and durability towards methanol oxidation. Nano Energy 2016;21:247–57.